Astronomy & Astrophysics manuscript no. main
November 11, 2026
©ESO 2026

Euclid Data Release 1 (DR1)

Euclid Lens Identification Pipeline and Scientific Exploration (ECLIPSE) C: Lens modelling pipeline overview

Euclid Collaboration: J. W. Nightingale, S. H. Vincken, L. R. Ecker, A. Nersesian, D. J. Bowden, C. M. O'Riordan, N. E. P. Lines, T. E. Collett, et al.

(Full author list and affiliations details can be found after the references)

ABSTRACT

Galaxy-scale strong lenses provide precise measurements of galaxy mass distributions, magnified views of distant galaxies, and a competitive cosmological probe. Historically, such studies have been limited to hundreds of lenses, with automated modelling methods proving difficult to scale. We present automated lens modelling of 15 072 strong-lens candidates from Euclid Data Release 1 (DR1), over an order of magnitude larger than any previously modelled sample. Using `PyAutoLens-JAX`, we perform three fits with multi-Gaussian expansion (MGE), pixelised, and Sérsic representations of the source, adopting an isothermal ellipsoid mass model with external shear. These fits provide foreground lens-light subtraction, adaptive Delaunay source reconstructions, and deblended photometry. More than 20 expert inspectors visually assess the resulting models, and each model is assigned the classification on which at least 75% of its inspectors agree. Of the 6073 grade A (secure) lens candidates, inspectors classify 4098 (67.5%) as successfully modelled, 580 (9.6%) as failures, 317 (5.2%) as multi-galaxy lenses, 15 (0.2%) as double-source-plane lenses, and 7 (0.1%) as unsure if lens, while 1032 (17.0%) reach no consensus and 24 (0.4%) have incomplete models. For the 8999 grade B (probable) candidates, the modelling success rate falls to 43.1%, primarily reflecting an increase in cases without consensus (37.6%), rather than a comparable increase in agreed failures (12.9%). We attribute this greater disagreement to uncertainty over whether these candidates are genuine lenses. For 2990 candidates, inspectors also record why models failed. Of the 210 failures, they attribute 39 (18.6%) to preprocessing and segmentation errors, 66 (31.4%) to inaccurate MGE lens-light subtraction, and 12 (5.7%) to source-reconstruction or mass-model failures, while 93 (44.3%) reach no consensus on the failure mode. Successfully modelled grade A and B systems have a median effective Einstein radius of $0\farcs85$ and a median total $I_{\rm E}$-band source magnification of 8.1. We publicly release the successful lens models, their inferred properties, and magnified-source reconstructions through the ECLIPSE catalogue, demonstrating automated modelling at *Euclid* sample sizes and enabling population-level strong-lensing science.

Key words. Gravitational lensing: strong, Methods: data analysis, Methods: statistical

1. Introduction

Galaxy-scale strong gravitational lensing occurs when a foreground galaxy aligns closely along the line of sight with a more distant background source. The mass of the foreground galaxy curves space-time, deflecting and magnifying the light of the source into multiple images, arcs, or, in the most aligned configurations, complete Einstein rings (Kochanek 2006; Treu 2010). Each such system encodes an unusually rich set of astrophysical measurements: the total mass and dark matter distribution of the foreground galaxy (Bolton et al. 2008; Vegetti et al. 2014; Oguri et al. 2014; Sonnenfeld et al. 2015), and a magnified view of a high-redshift source that would otherwise be inaccessible (Swinbank et al. 2015; Atek et al. 2015; Dye et al. 2018; Rizzo et al. 2020; Amvrosiadis et al. 2025). Strong lenses also provide cosmological constraints on the Hubble constant through time delays (Suyu et al. 2017; Wong et al. 2020; Birrer et al. 2020), the matter density and dark energy through double-source-plane systems (Collett & Auger 2014; Sahu et al. 2025; Euclid Collaboration: Li et al. 2026), and cosmic shear through line-of-sight perturbations (Birrer et al. 2017, 2018; Hogg et al. 2026; Fleury et al. 2026), for which *Euclid*'s upcoming weak-lensing catalogue further enables cross-correlations with galaxy shapes and tests for systematic errors in shear measurements (Hogg et al. 2023; Fleury et al. 2026).

Extracting that information requires strong lens modelling, a simultaneous analysis of the light of the foreground lens galaxy, its mass distribution, and the unlensed surface brightness of the background source. Conceptually, a model of the light of the source is forward ray-traced via general relativity, with its path distorted by a mass model of the foreground lens galaxy. This produces an image of the lensed source, which is added to a model image of the light of the foreground lens and compared to the data. Lens modelling puts this process in an inference procedure, varying the model parameters to determine the combination of lens light, mass, and source light that best reproduces the observed strong lens system (e.g. Warren & Dye 2003; Suyu et al. 2006; Vegetti & Koopmans 2009; Nightingale et al. 2018; Birrer & Amara 2018; Vernardos & Koopmans 2022; Galan et al. 2022); see also the review by Shajib et al. (2024).

As strong lens samples have grown, scaling lens modelling has posed a significant challenge. Dedicated strong lens surveys discovered hundreds of lenses (Bolton et al. 2008; Treu et al. 2011; Brownstein et al. 2012; Gavazzi et al. 2014; Shu et al. 2016; Tran et al. 2022), with modelling performed successfully but typically on a lens-by-lens basis using procedures that relied heavily on manual human intervention. Automated and uniform modelling pipelines have since been introduced (Nightingale et al. 2018, 2021) and demonstrated on real data (Shajib et al. 2019; Etherington et al. 2022; Schuldt et al. 2023), al-

though these relied on manual preprocessing steps that have only recently been automated (Shajib et al. 2025; Euclid Collaboration: Vincken et al. 2026a). Automated modelling has also been demonstrated for lensed quasars (Ertl et al. 2023; Schmidt et al. 2023). Despite the availability of samples containing hundreds of strong lenses, automated modelling studies have generally been demonstrated on fewer than about 100 systems, highlighting the difficulty of scaling lens modelling to survey-sized data sets. Nightingale et al. (2025) present lens models for 419 strong lens candidates discovered with the *James Webb* Space Telescope as part of the COSMOS-Web Lens Survey (COWLS).

The *Euclid* mission (Euclid Collaboration: Scaramella et al. 2022; Euclid Collaboration: Mellier et al. 2025) will provide high-resolution imaging from its visible instrument (VIS), with a pixel scale of 0.″1 and point-spread function (PSF) full width at half maximum (FWHM) of approximately 0.″16 (Euclid Collaboration: Cropper et al. 2025; Euclid Collaboration: McCracken et al. 2026a), across 14 000 deg^2 of sky, alongside three near-infrared bands from its Near-Infrared Spectrometer and Photometer (NISP) that provide crucial colour information (Euclid Collaboration: Jahnke et al. 2025). This combination of image quality and survey scale is expected to yield in excess of 100 000 galaxy-scale strong lenses (Collett 2015), transitioning strong lensing into the era of large statistical samples. The precise number depends on the lens and source populations assumed and on how lenses are identified (Holloway et al. 2023; Ferrami & Wyithe 2024). The VIS imaging is sufficiently resolved to measure key lensing quantities directly from the data, including Einstein radii, lens-galaxy mass distributions, and the morphologies of lensed source galaxies.

Euclid DR1 (Euclid Data Release 1), covering approximately 2000 deg^2, already represents a major step towards this goal and is expected to contain more strong lenses than all previous samples combined. Automated modelling of *Euclid* lenses has already been demonstrated on the Early Release Observations (Acevedo Barroso et al. 2025; O'Riordan et al. 2025) and, at larger scale, by the Strong Lens Discovery Engine (SLDE) collaboration on approximately 500 grade A and B lenses discovered in Q1 (Euclid Collaboration: Walmsley et al. 2026; Euclid Collaboration: Rojas et al. 2026; Euclid Collaboration: Lines et al. 2026b; Euclid Collaboration: Li et al. 2026; Euclid Collaboration: Holloway et al. 2026a; Euclid Collaboration: Ecker et al. 2026). Grade A denotes a secure lens with unambiguous lensing features, and grade B a probable lens requiring additional evidence to confirm its lensing nature. In the ECLIPSE catalogue and discovery pipeline (Euclid Collaboration: Lines et al. 2026a; Euclid Collaboration: Holloway et al. 2026b), both grades are assigned solely from visual inspection of the imaging, before lens modelling.

This paper presents strong lens modelling results for 15 072 grade A and B strong-lens candidates discovered across the Euclid DR1 footprint as part of the ECLIPSE survey (Euclid Collaboration: Lines et al. 2026a), the first end-to-end strong-lens discovery and characterisation effort at this scale. In doing so, we address a long-standing question in strong lensing: can strong lens modelling be scaled beyond thousands of lenses? To quantify how often modelling succeeds at this scale, the Euclid Strong Lensing Science Working Group (SL-SWG) performed a dedicated visual inspection campaign involving over 20 expert lens modellers, with each inspected model assessed by at least four inspectors. This enables us to quantify the success rate of automated lens modelling, provide a catalogue of validated lens models for future scientific study,[1] and systematically identify the dominant failure modes of automated lens modelling.

For successfully modelled systems, we measure the principal lens and source properties to characterise the sample and provide a foundation for subsequent scientific studies. We first investigate the inferred Einstein radii which, when lens and source redshifts are known, can be converted into Einstein masses, widely regarded as among the most precise galaxy mass measurements in astronomy (see reviews by Treu 2010; Shajib et al. 2024), with systematic uncertainties of order 5% reported in previous work (Bolton et al. 2008). Here we characterise the distribution of inferred Einstein radii, providing a basis for future population studies (Sonnenfeld & Cautun 2021; Sonnenfeld 2021, 2022a). We also show the inferred source magnifications and make the source reconstructions for every successfully modelled lens publicly available across the high-resolution VIS imaging and all available NISP and external (EXT) ground-based wavebands. Lens modelling of galaxy-scale strong lenses has enabled a broad range of source-galaxy science (Swinbank et al. 2015; Dye et al. 2018; Rizzo et al. 2020; Amvrosiadis et al. 2025), and we aim to extend this capability to large samples.

This paper is part of a series describing the Euclid DR1 strong lens search and catalogue. Euclid Collaboration: Lines et al. (2026a, hereafter ECLIPSE-A) presents the catalogue of 15 072 grade A and B galaxy-scale strong lenses discovered across the DR1 footprint, the largest homogeneous strong lens sample assembled to date. The catalogue is the product of the discovery pipeline described by Euclid Collaboration: Holloway et al. (2026b, hereafter ECLIPSE-B), which combines machine-learning classification, citizen-science inspection, and expert visual validation to identify strong lenses from approximately 68 million galaxies. Companion analyses of photometric redshifts and the physical properties of the deflector galaxies are presented in Euclid Collaboration: Nersesian et al. (2026, hereafter ECLIPSE-D). The automated segmentation and modelling inputs used here are presented by Euclid Collaboration: Vincken et al. (2026a) through `AstroVink-TREX`. This builds on the `AstroVink` vision-transformer lens-finding framework introduced for Euclid Q1 by Euclid Collaboration: Vincken et al. (2026b). Dedicated modelling of multi-galaxy lenses, in which more than one foreground galaxy contributes to the lensing, is presented by Euclid Collaboration: Wielders et al. (2026).

The remainder of this paper is organised as follows. Section 2 describes the Euclid DR1 imaging and strong-lens candidate sample. Section 3 sets out the automated preprocessing applied to each lens prior to modelling. Section 4 defines the lens model and the three-fit procedure. Section 5 details the visual inspection campaign, and Sect. 6 presents the catalogue together with the success and failure statistics and the multi-wavelength results. We discuss the implications in Sect. 7 and summarise in Sect. 8.

2. Data

ECLIPSE-A describes how lens candidates come from a search of the approximately 2000 deg^2 DR1 footprint. The primary data used for lens modelling are the high-resolution images from the *Euclid* VIS instrument (Euclid Collaboration: Cropper et al. 2025), observed through the broad optical $I_{\rm E}$ filter. The VIS imaging provides the optimal data for lens modelling because of its high spatial resolution and diffraction-limited image quality. The data were accessed via the European Space Agency (ESA)

[1] `https://euclid-eclipse-lenses.org`

Science Archive Service and ESA Datalabs.[2] For each lens candidate, we extracted 100×100 pixel cutouts, corresponding to $10''.0 \times 10''.0$ at the VIS pixel scale of $0''.1$ pixel^{-1}. These cutouts included the science image, root mean square (RMS) noise map, and PSF, all of which were used in the lens modelling.

We used the effective PSFs supplied by the *Euclid* MERge (MER) processing pipeline, which propagates the input PSF models through resampling and stacking to provide PSF stamps appropriate to each object's position and waveband (Euclid Collaboration: Romelli et al. 2026). For VIS, these combine the position-dependent PSF models of the contributing observations, accounting for the mosaicing process. We did not use the more detailed, colour-dependent PSF treatment developed for the shear-measurement (SHE) processing function (Euclid Collaboration: McCracken et al. 2026b). Using this PSF, we measured Einstein radii, lens-light properties, and source reconstructions, constrained by the positions and appearance of the lensed images together with the foreground light distribution. However, higher-fidelity PSFs may be required for more complex lens models, such as power-law mass profiles that constrain the radial density slope. We recommend that readers planning to fit more complex lens models to the public data first contact the SL-SWG for current guidance on PSF limitations and other data-reduction issues. Improvements in these areas are expected following this work.

Following the VIS fit, lens modelling was performed independently in each additional waveband using the NISP near-infrared imaging (Euclid Collaboration: Jahnke et al. 2025) and EXT ground-based data, for photometric-redshift estimation and spectral energy distribution (SED) fitting. The MER NISP and EXT images and their corresponding PSFs are sampled on the same $0''.1$ pixel^{-1} grid as VIS; no additional PSF subsampling was applied during lens modelling. The multi-wavelength modelling approach and example NISP and EXT modelling results are presented in ECLIPSE-D.

3. Preprocessing

Before lens modelling, each lens image was preprocessed to define the inputs required by the *Euclid* strong-lens modelling pipeline. These inputs are: (i) the circular mask, outside of which pixels are excluded from the likelihood evaluation; (ii) candidate conjugate points (image-plane positions at the brightest locations of the multiple images, assumed to correspond to the same source-plane location), which are used during fitting to reject mass models that do not trace the images to consistent source-plane positions (Maresca et al. 2021); and (iii) a binary mask flagging nearby galaxies whose emission overlaps the fitting region and must therefore be removed. Historically, these tasks have been performed manually by the scientist using one or more graphical user interfaces (GUIs), as in Nightingale et al. (2025).

To automate preprocessing for thousands of lenses, we used the machine-learning framework of Euclid Collaboration: Vincken et al. (2026a), which segments foreground lens light, lensed source emission, and nearby galaxies (Fig. 1). The brightest pixel in the predicted lens-light map defined the fitting-mask centre, lens-light centre priors, and initial mass-model centre, subsequently refined using the nearby VIS light. For the initial multi-Gaussian expansion (MGE) fit, the lens-light centre had a uniform prior spanning $\pm 0''.1$ in each coordinate around this refined centre. The circular fitting mask extended $2''.0$ beyond

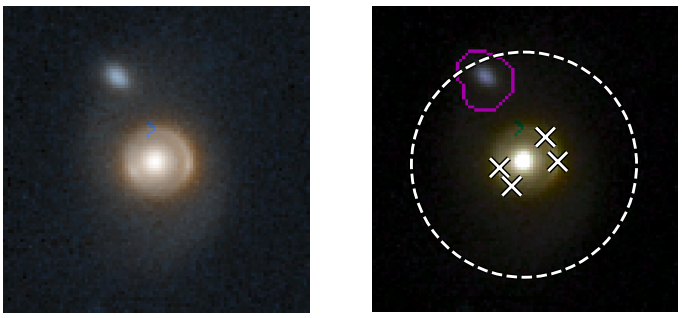


Fig. 1. Example results of automated preprocessing for the lens Euclid-DR1 J030313.592−580619.97. North is up and east is to the left, as in all images in this paper. *Left*: An RGB image using one colour scaling that contrasts the lens and source light with that of a nearby galaxy to the north-east. *Right*: An RGB image with different colour scaling that shows the fitting mask, candidate conjugate points, and contaminating-galaxy contour used in lens modelling. The white dashed circle shows the fitting mask, whose radius is computed from the furthest pixel in the segmented source emission, plus an additional buffer. White crosses with black outlines mark the automatically identified candidate conjugate points. The magenta contour marks a nearby contaminating galaxy whose light overlaps the fitting region and is therefore effectively excluded from the likelihood by zeroing its data values and inflating its RMS values.

the segmented source emission, whose brightness peaks provided candidate conjugate points. Contaminating galaxies were effectively excluded from the likelihood by zeroing their data values and setting their RMS values to 10^8 in the image's flux units, while retaining their pixels for ray tracing to avoid discontinuities in the source-plane mesh (Etherington et al. 2022, section 4.3.2).

To constrain multiple images to originate from a common source, candidate conjugate points were ray-traced at each likelihood evaluation, penalising models whose maximum pairwise source-plane separation exceeded a specified threshold. Below this threshold the points did not affect the likelihood; above it, a penalty proportional to the excess separation was subtracted from the log-likelihood, with the threshold for the first fit set between $0''.3$ and $0''.5$ from a pre-fit to the points (Appendix A.5). The candidate points taken from the segmentation can occasionally miss images, for example when a counter-image lies close to the lens centre, and can link peaks from different regions of the source plane. We therefore updated them during the *Euclid* strong-lens modelling pipeline (Sect. 4.5).

4. Lens modelling

4.1. Overview

We used version `2026.10.7.1` of the lens modelling software `PyAutoLens` (Nightingale et al. 2021).[3] `PyAutoLens` simultaneously fits the light and mass of the lens galaxy and the source galaxy. The method assumes a model for the foreground light of the lens, which accounts for blurring by the instrumental PSF and is subtracted from the observed image. A mass model ray-traces image pixels from the image plane to the source plane, where either a parametric source model or a pixelised source reconstruction on a Delaunay mesh is fitted. Jupyter notebooks providing a visual step-by-step guide to the `PyAutoLens` likeli-

[2] `https://datalabs.esa.int/`

[3] `https://github.com/PyAutoLabs/PyAutoLens`

hood function used in this work are available online.[4] The *Euclid* strong-lens modelling pipeline used in this work, implemented in `PyAutoLens`, is publicly available.[5]

We fitted the lens light, mass distribution, and background source simultaneously using the semi-linear inversion framework (Warren & Dye 2003). The model comprises 15, 10, and 12 non-linear free parameters in the MGE, pixelised, and Sérsic fits (Sect. 4.5), describing the lens mass, external shear, light-profile geometry, and source regularisation, which were sampled using the nested sampler `nautilus` (Lange 2023). At each likelihood evaluation, the foreground lens-light and background source intensities were solved jointly as non-negative linear parameters, so the potentially large number of Gaussian amplitudes and source-pixel intensities need not be sampled non-linearly, substantially reducing the dimensionality of the non-linear parameter space.

For accelerated inference, we used `PyAutoLens-JAX` (Nightingale et al., in preparation), which supports execution on both CPUs and GPUs. We used CPUs for this analysis because CPU hardware was more readily available and inference time was not a limiting factor. For the full 15 072-candidate analysis, we also used `PyAutoLens-Assistant`,[6] a natural-language interface that assists users in setting up and managing lens-modelling workflows. Its development was informed by our experience modelling an initial subset of 2990 candidates from the Euclid DR1 catalogue.

Figure 2 shows an overview of a `PyAutoLens` lens model using the lens candidate Euclid-DR1 J030313.592−580619.97. The figure summarises the main components of the `PyAutoLens` fit: the observed VIS image, the lens light and source model images, the lens-subtracted lensed source, the fit residuals, and the reconstructed source plane with different degrees of zooming. The mask used in this figure corresponds to the white circle in Fig. 1 and the extra galaxy marked by the magenta contour in Fig. 1 is visible in Fig. 2 as zeroed pixels in the VIS data panel and a corresponding region with zero signal-to-noise ratio. This masking removes the contaminating galaxy from the likelihood while retaining the lensed source emission used to constrain the model. The white curves show the tangential critical curve in the image plane and the corresponding caustic in the source plane.

4.2. Lens light modelling

We modelled the foreground lens light using an MGE (Cappellari 2002), comprising a sum of two-dimensional elliptical Gaussian profiles, following He et al. (2024, hereafter H24). The MGE provides a flexible and computationally efficient representation of the lens galaxy emission, well suited to automated modelling of large strong-lens samples. Appendix A details the MGE equations, width convention, and joint linear solution.

We modelled the lens light using two sets of 20 Gaussians with logarithmically spaced widths, sharing a common centre but with independent axis ratios and orientations, giving six non-linear parameters. While H24 used up to six sets of 30 Gaussians for HST imaging, our tests on *Euclid* data found that two sets improved the fits over one, particularly for S0 galaxies with distinct bulge and disc components. We therefore adopted two sets as a compromise between flexibility and computational efficiency, with visual inspection (Sect. 5) used to identify inadequate lens-light models.

4.3. Mass profile

For the lens mass model, we assumed a singular isothermal ellipsoid (SIE) density profile of the form

$$\kappa(\xi) = \frac{1}{1 + q^{\rm mass}} \left(\frac{\theta_{\rm E}^{\rm mass}}{\xi} \right), \tag{1}$$

where $q^{\rm mass}$ is the mass-profile axis ratio, $\xi = \sqrt{x'^2 + (y'/q^{\rm mass})^2}$ is the elliptical radius in lens-centred coordinates aligned with the mass distribution, and $\theta_{\rm E}^{\rm mass}$ is the model Einstein radius in arcseconds. Deflection angles were computed via an implementation of the method of Tessore & Metcalf (2015) in `PyAutoLens`.

We included external shear, a standard approximation for tidal perturbations from matter outside the main lens galaxy. It is described by a magnitude, $\gamma^{\rm ext}$, and an orientation, $\phi^{\rm ext}$, measured anticlockwise from the $+x$ axis of the modelling grid. In the fit we used the two components $(\gamma_1^{\rm ext}, \gamma_2^{\rm ext})$, related to these quantities by

$$\gamma_1^{\rm ext} = \gamma^{\rm ext} \cos(2\phi^{\rm ext}) \,, \qquad \gamma_2^{\rm ext} = \gamma^{\rm ext} \sin(2\phi^{\rm ext}) \,. \tag{2}$$

The deflection angles due to external shear were computed analytically. However, the fitted shear can also absorb missing complexity in the lens mass distribution (Etherington et al. 2024), so it need not represent a physical measurement of the external tidal field.

The catalogue reports the effective Einstein radius, denoted $\theta_{\rm E}$ below, defined for non-axisymmetric lenses as

$$\theta_{\rm E} = \sqrt{\frac{A_{\rm crit}}{\pi}} \,, \tag{3}$$

where $A_{\rm crit}$ is the angular area enclosed by the tangential critical curve. Because this area is measured from the full SIE plus external-shear model, the reported $\theta_{\rm E}$ includes the shear contribution to the critical-curve geometry and is not identical to the SIE scale parameter $\theta_{\rm E}^{\rm mass}$.

4.4. Source model

We modelled the background source using three representations: a multi-Gaussian expansion (Cappellari 2002; He et al. 2024), a pixelised Delaunay reconstruction, and an elliptical Sérsic profile. The pixelised reconstruction combines Hilbert-based adaptive mesh placement (He et al. 2025), barycentric interpolation (Vegetti & Koopmans 2009; Vernardos & Koopmans 2022), and adaptive split regularisation (Nightingale et al. 2024; He et al. 2024), whose strength was inferred alongside the lens mass parameters (Warren & Dye 2003; Suyu et al. 2006). We evaluated PSF-convolved models using a Gaussian-noise likelihood, with spatially adaptive oversampling of the lens and source light (Nightingale et al. 2024). Appendix A provides the forward-model, joint linear solution, adaptive mesh, regularisation, and likelihood equations.

The source magnification, μ, is computed as the ratio of the lensed source flux in the image plane, $F_{\rm lensed}$, to its intrinsic source-plane flux, $F_{\rm source}$,

$$\mu = \frac{F_{\rm lensed}}{F_{\rm source}} \,. \tag{4}$$

[4] `https://github.com/Jammy2211/autolens_likelihood_function`

[5] `https://github.com/PyAutoLabs/euclid_strong_lens_modeling_pipeline`

[6] `https://github.com/PyAutoLabs/autolens_assistant`

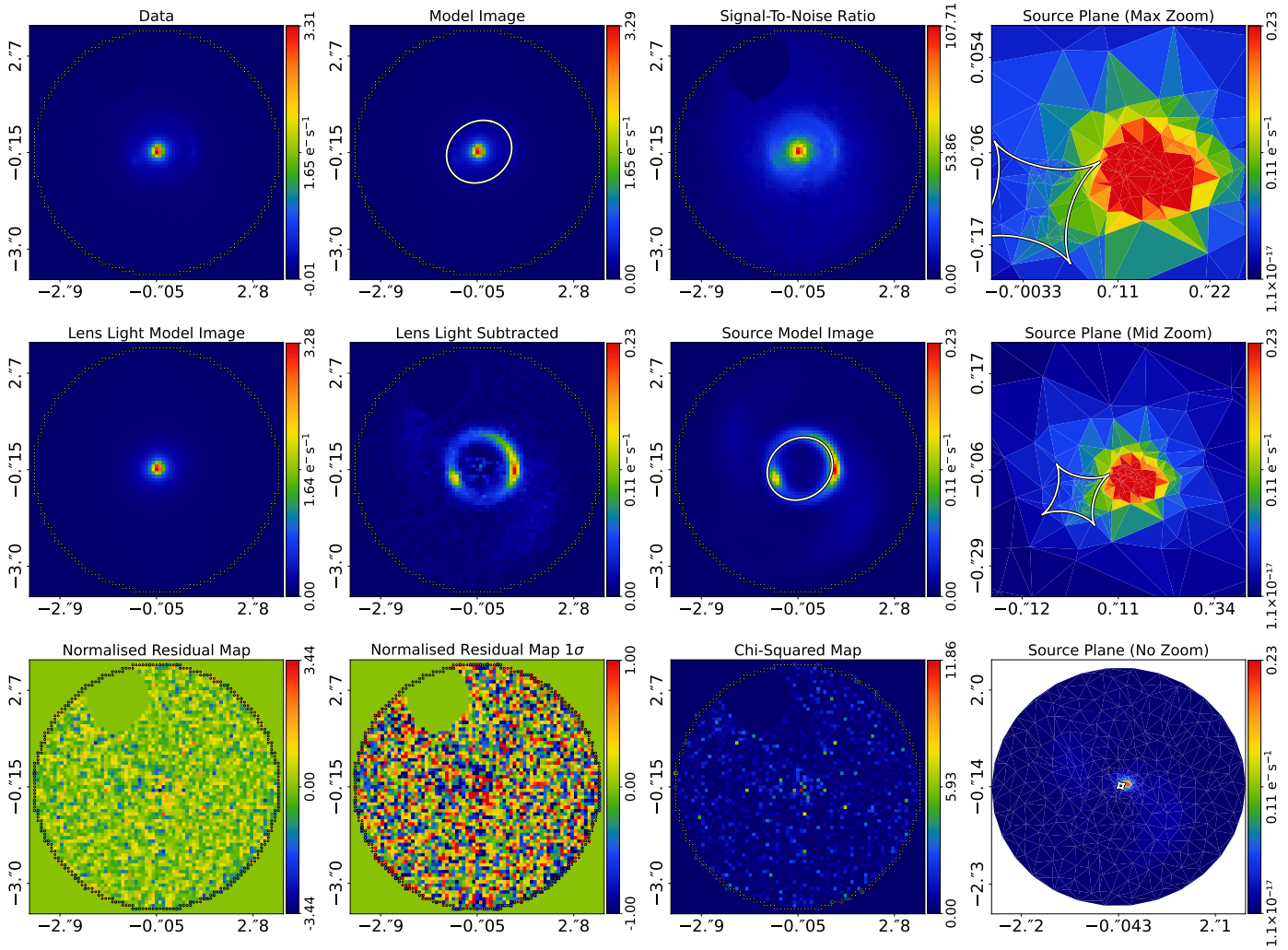


Fig. 2. Example VIS `PyAutoLens` lens-model summary for the lens candidate J030313.592−580619.97, the same system shown in Fig. 1. The top row shows, from left to right, the VIS data, the full model image, the signal-to-noise ratio map, and a maximally zoomed view of the reconstructed source plane. The middle row shows the foreground lens-light model, the lens-subtracted image, the lensed source model image, and a mid-zoom source-plane reconstruction. The bottom row shows the normalised residual map, the same residual map plotted in the range from -1σ to $+1\sigma$, the χ^2 map, and the full source-plane reconstruction. The zeroed regions in the maps correspond to the contaminating galaxy marked by the magenta contour in Fig. 1. White dots with black edges mark the image-plane mask boundary, while white curves with black outlines show the critical curve and caustic structure where plotted.

The magnifications quoted in this paper use the Sérsic source model to facilitate comparison with previous literature and standard galaxy photometry (see ECLIPSE-D); the catalogue also includes magnifications derived from the Delaunay source reconstruction.

4.5. Sequential lens model fits

The pipeline comprises three fits with complementary purposes. The first used MGE lens and source light to establish an initial mass model and foreground-light subtraction. The second used a flexible pixelised source to refine the mass model and reconstruct the source morphology. The third held the first-fit mass model fixed and fitted Sérsic light profiles to obtain deblended photometry and structural measurements of the lens and source. Appendix A gives the likelihood equations, and Table A.1 summarises the free and fixed quantities in each stage. The explicit priors and sampler settings are given in Appendix A.6. Each search stopped on meeting the `nautilus` convergence criteria or reaching its likelihood-evaluation limit; reaching that limit does not itself establish convergence.

The first fit used MGEs (Cappellari 2002; He et al. 2024) for both the lens and source light, together with an SIE mass profile and external shear (see Sect. 4.3), and was performed with the nested sampler `nautilus` (Lange 2023).[7] The intensities of the MGE light profiles for the lens and source were solved for linearly using the semi-linear inversion. For the source, we used one set of 20 Gaussians, whose σ values spanned a base-10 logarithmic range from 0.″0001 to the mask radius.

After inference with the simpler parametric MGE source model was complete, the conjugate points were updated using its maximum-likelihood mass model, recovering missed images and replacing peaks associated with different source regions with positions corresponding to a common source location. The threshold used in the second fit was then reset to three times the maximum source-plane separation of the updated points un-

[7] `https://github.com/johannesulf/nautilus`

der this mass model, with a minimum of 0″.2 (Etherington et al. 2022, section 4.3.2).

The second fit, also performed with `nautilus`, replaced the parametric source model with a Delaunay mesh source reconstruction, while retaining an MGE for the lens light and an SIE mass profile with external shear. The non-linear parameters of the MGE lens light model were fixed to the values inferred in the first fit, but the Gaussian intensities were re-solved linearly for every model evaluated alongside the source reconstruction. The second fit released the SIE centre within 0″.1 of the data set centre in each coordinate. Its SIE shape, Einstein-radius, and shear priors were not narrowed using the first-fit posterior; Table A.2 specifies their distributions, including the non-uniform priors on the SIE ellipticity components.

The third fit was performed to obtain deblended photometry of the lens and source galaxies. The maximum-likelihood mass model inferred from the first fit was fixed, and the MGE light profiles of both the lens and source were replaced with elliptical Sérsic profiles. This fit was performed on the VIS imaging, where the structural parameters of the lens and source light profiles were inferred. Lens and source magnitudes were computed from the total flux of the foreground Sérsic lens model and the lensed Sérsic source model in the image plane, respectively. The source magnification reported in the catalogue was then computed using Eq. (4), with the SIE mass model and external shear fixed from the initial MGE fit. In ECLIPSE-D, the same fixed mass model with Sérsic lens and source was then used to fit each available NISP and EXT waveband independently for deblended photometry, photometric-redshift estimation, and SED fitting.

5. Visual inspection

The goals of this visual inspection campaign were (i) to produce a catalogue of galaxy-scale lenses whose models a majority of experts agree are robust and accurate for subsequent scientific study; (ii) to quantify the overall success rate of the automated lens modelling pipeline; and (iii) to understand and categorise the reasons why lens modelling fails, thereby guiding future automated lens modelling efforts. More than 20 lens-modelling experts participated in the visual inspection campaign for the DR1 sample of 15 072 candidates.

A preliminary round of visual inspection, described in Appendix B, was undertaken in which 12 expert inspectors reviewed 200 lens models. The results of this exercise, together with follow-up discussion amongst the inspectors, were used to refine the criteria defining a successful lens model, determine the categories used to describe modelling failures, and identify the diagnostic images most informative for assessing model quality. This enabled the final inspection GUI used for 15 072 lenses to present the minimum amount of information necessary to balance inspection speed with diagnostic power.

For the main visual inspection campaign, inspectors were shown two diagnostic images for each candidate: (i) the RGB image with segmentation information, as shown in Fig. 1, and (ii) the lens-model overview image shown in Fig. 2. Together, these provided the colour information needed to distinguish lens and source emission, as well as the modelling diagnostics required to assess whether the data are successfully fitted by a lens model. Figure 2 shows the Delaunay source reconstruction shown to inspectors by default. Inspectors assigned classifications based solely on the Delaunay modelling results. They could also switch in the GUI to a parametric MGE source model for supplementary diagnostic information, but did not classify the MGE fits. Sérsic fits were omitted because their close resemblance to the MGE fits would add redundant information and risk confusion.

The source-plane panels retain the zoom levels used during visual inspection (Fig. 2), which are occasionally suboptimal (e.g. zoomed in too far to show the full source). Each Delaunay triangle is displayed with a single colour to illustrate the mesh resolution, although the underlying source reconstruction is continuous through piecewise-linear barycentric interpolation (Appendix A.3).

5.1. Inspection classifications

The five primary classification options available to inspectors were “Success” (SC), “Failure” (FL), “Unsure If Lens” (UIL), “Double Source Plane Lens” (DSPL), and “Multi Galaxy Lens” (MGL). During preliminary inspection, it was noted that the sample contained systems that violate the modelling assumptions in two common ways. In a DSPL system, multiple sources at different redshifts are lensed by the same foreground deflector; in an MGL system, more than one lens galaxy lies within the Einstein radius. The automated modelling pipeline assumes a single MGE lens light model, a single SIE mass profile, and a single source plane; these systems are therefore not expected to be modelled accurately. The visual inspection procedure therefore instructed reviewers to identify DSPL and MGL systems as standalone categories in the initial classification stage.

Using the diagnostic images, inspectors assigned these classifications according to the following criteria:

1. You have high confidence that the object is a genuine strong gravitational lens (otherwise classify it as UIL).
2. The system does not contain sources at multiple redshifts (otherwise classify it as DSPL).
3. The system contains only one lens galaxy within its Einstein radius (otherwise classify it as MGL).
4. The lens model provides an accurate and reliable measurement of the Einstein radius suitable for publication in a peer-reviewed scientific article (otherwise classify it as FL).
5. The critical-curve morphology and source reconstruction are physically plausible (otherwise classify it as FL).
6. If all criteria above are satisfied, classify the system as SC.

For a subset of 2990 lens candidates, inspectors were additionally asked to identify the reason for unsuccessful lens models. When classifying a model as a failure (FL), inspectors selected one of three categories: segmentation/masking (FL-Segmentation), lens-light subtraction (FL-LensLight), or source reconstruction/mass modelling (FL-SourceMass). Inspectors were instructed to consider these categories sequentially and select the first applicable failure, reflecting how errors propagate through the modelling pipeline. For example, incorrect segmentation can lead to poor lens-light subtraction, which can in turn cause the source reconstruction to fit residual lens light rather than genuine source emission. The source reconstruction/mass modelling category was reserved for cases where earlier stages were successful but the reconstructed source or inferred mass model was physically implausible. This structured approach was introduced following preliminary inspections, where less constrained classifications proved difficult to interpret.

The number of recorded votes varied from four to seven per inspected object. Detailed reasons for failure were not requested in the main campaign of all 15 072 objects because of inspector

Table 1. Key to the primary inspection classifications and the consensus outcome.

Code	Classification	Description
SC	Success	Confident lens identification, a reliable Einstein radius, and physically plausible critical curves and source reconstruction; single-deflector, single-source-plane criteria satisfied.
FL	Failure	Confident lens identification satisfying the single-deflector and single-source-plane criteria, but the model fails the reliability or physical-plausibility criteria.
UIL	Unsure If Lens	Insufficient confidence that the candidate is a genuine strong lens.
DSPL	Double Source Plane Lens	Multiple sources at different redshifts lensed by the same foreground deflector.
MGL	Multi Galaxy Lens	More than one lens galaxy within the Einstein radius.
NC	No Consensus	No unique primary classification satisfies the adopted consensus rule; assigned from the combined votes.
–	Incomplete	No completed pixelised model; not inspected.

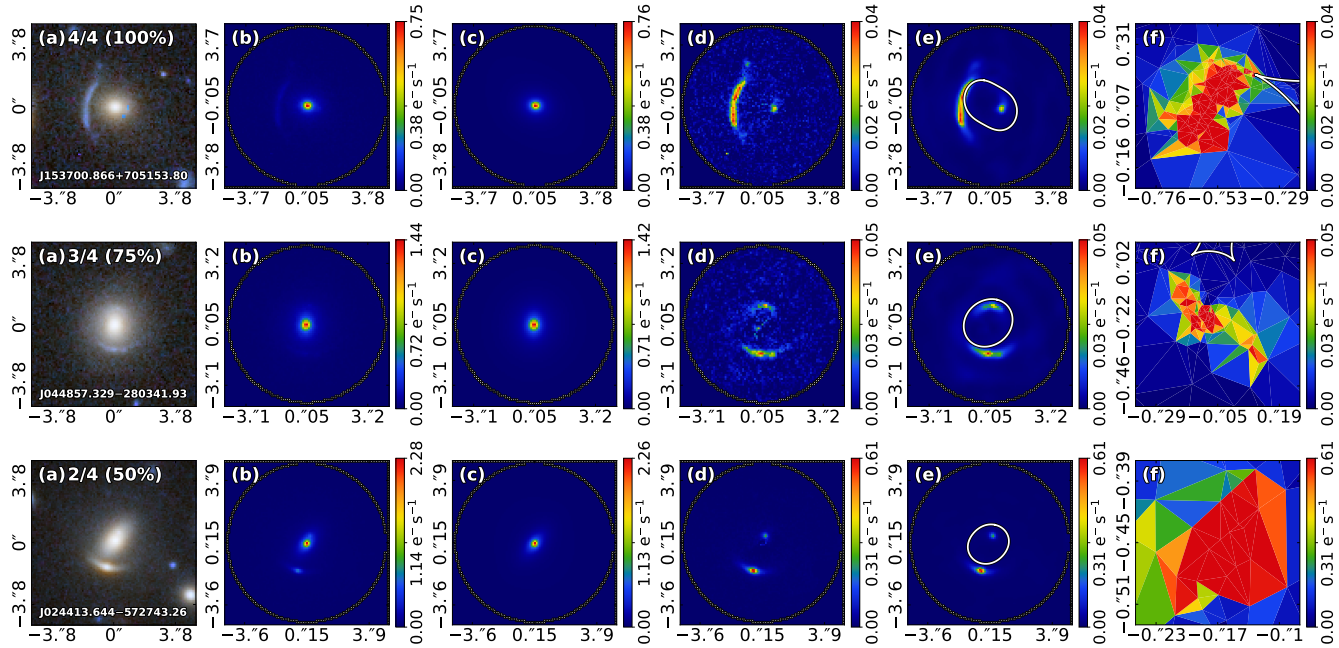


Fig. 3. Representative grade A Success (SC) lens models spanning the observed SC-vote fractions. The systems in the top, middle, and bottom rows have 4/4 (100%), 3/4 (75%), and 2/4 (50%) SC votes, respectively; the bottom system is NC at the adopted 75% threshold. Individual candidates were reviewed by subsets of the inspection team, so each RGB panel gives both the SC-vote tally and its fraction. Within each row, the panels show (a) the RGB image, (b) the VIS data, (c) the foreground lens-light model, (d) the lens-subtracted image, (e) the lensed source-model image, and (f) the source-plane reconstruction. Images are north up, east left; axes give offsets in arcseconds, with y increasing to the north and x to the west. White dots mark the fitting mask; critical curves and caustics have black outlines. The higher-agreement examples have plausible lens-light subtraction and source reconstructions, whereas the lower-agreement example illustrates the greater ambiguity introduced at lower consensus thresholds. Fourteen additional examples are shown in Fig. C.1.

time constraints. Table 1 summarises the five primary classifications, together with the outcome assigned when inspectors did not reach consensus, defined in Sect. 5.2.

5.2. Consensus thresholds

All inspectors had equal voting weight, with no individual veto. We assigned a consensus classification when at least a specified fraction of inspectors agreed; otherwise, the object was labelled "No Consensus" (NC). This was determined from the combined votes rather than being an option available to individual inspectors. At our adopted 75% threshold, three of four, four of five, or five of six inspectors had to agree. We applied this threshold independently to the five primary classifications (SC, FL, UIL, DSPL, and MGL) and the secondary failure categories (FL-Segmentation, FL-LensLight, and FL-SourceMass) recorded for the 2990-candidate sample. Primary classifications required a unique consensus. At the 50% threshold, ties between classifications were assigned NC. At the adopted 75% threshold, no two primary classifications can simultaneously meet the threshold. For secondary failure modes, ties were instead resolved in the causal order FL-Segmentation, FL-LensLight, then FL-SourceMass. No minimum number of votes was imposed, while objects without recorded votes received no classification but are included in the totals from which success rates are calculated.

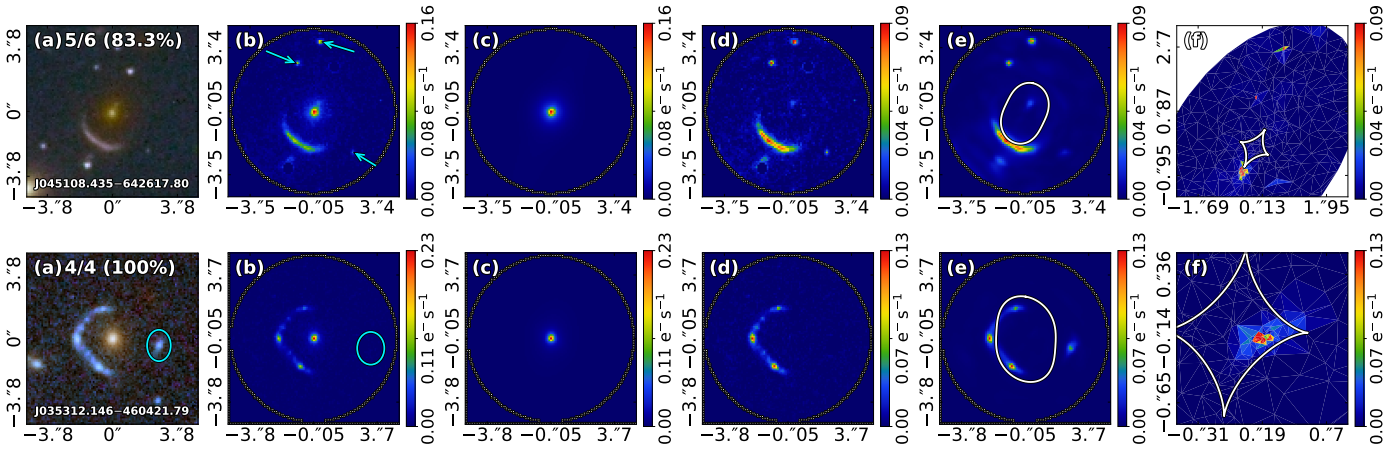


Fig. 4. Grade A Success (SC) models above the 75% SC consensus threshold despite residual segmentation issues. Panels follow the same layout as Fig. 3. In the top row, cyan arrows in panel (b) identify unmasked nearby objects whose light is mapped into the source reconstruction. In the bottom row, cyan ellipses in panels (a) and (b) highlight part of a genuine multiple image that is visible in the RGB image but incorrectly masked in the VIS data. The ellipses are visual guides rather than exact mask boundaries. The inferred Einstein radii remain reliable, but these issues limit the use of the models for detailed source reconstruction or more complex mass modelling.

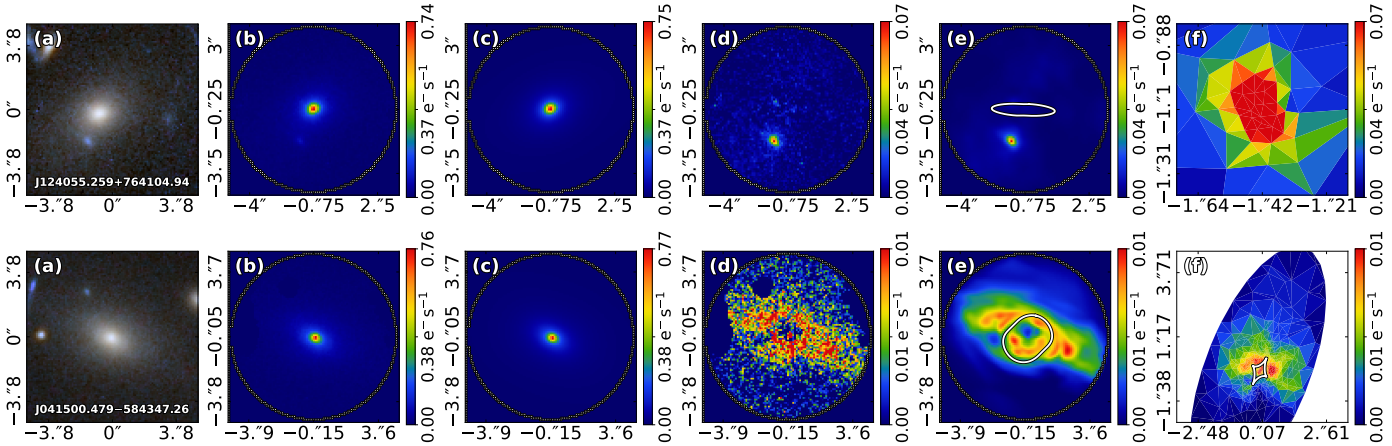


Fig. 5. Two grade A Unsure If Lens (UIL) systems, each with 100% UIL agreement in the inspection campaign. Panels follow the same layout as Fig. 3. From top to bottom, the examples illustrate a missing counter-image and faint residual emission with insufficient signal-to-noise ratio to establish a convincing lens.

Table 2. Primary inspection classifications at each consensus threshold for grade A (N = 6073) and grade B (N = 8999). Entries give counts and, in parentheses, percentages of all objects of the corresponding grade. Incomplete: candidates without a completed pixelised model, which were not inspected. SC: Success; UIL: Unsure If Lens; DSPL: Double Source Plane Lens; MGL: Multi Galaxy Lens; FL: Failure; NC: No Consensus. Ties at 50% are NC.

Grade	Threshold	SC	UIL	DSPL	MGL	FL	NC	Incomplete
A	100%	3011 (49.6%)	3 (<0.1%)	1 (<0.1%)	172 (2.8%)	272 (4.5%)	2590 (42.6%)	24 (0.4%)
	75%	4098 (67.5%)	7 (0.1%)	15 (0.2%)	317 (5.2%)	580 (9.6%)	1032 (17.0%)	24 (0.4%)
	50%	4411 (72.6%)	24 (0.4%)	25 (0.4%)	394 (6.5%)	788 (13.0%)	407 (6.7%)	24 (0.4%)
B	100%	2163 (24.0%)	16 (0.2%)	1 (<0.1%)	179 (2.0%)	362 (4.0%)	6219 (69.1%)	59 (0.7%)
	75%	3882 (43.1%)	123 (1.4%)	4 (<0.1%)	385 (4.3%)	1161 (12.9%)	3385 (37.6%)	59 (0.7%)
	50%	4827 (53.6%)	434 (4.8%)	19 (0.2%)	571 (6.3%)	1896 (21.1%)	1193 (13.3%)	59 (0.7%)

6. Results

Table 2 reports the SC, UIL, DSPL, MGL, FL, and NC counts for grades A and B separately under thresholds of 100%, 75%, and 50%. For 83 candidates, no completed pixelised model is available; these were not inspected and are listed as incomplete. The diagnostic figures in this section use a reduced set of panels for visual presentation in this paper. These are not the full diagnostic images used during the visual inspection campaign described in Sect. 5.

6.1. SC models

At the adopted 75% threshold (Sect. 5.2), 4098 of 6073 grade A candidates (67.5%) are classified as successfully modelled (SC), compared with 3882 of 8999 grade B candidates (43.1%).

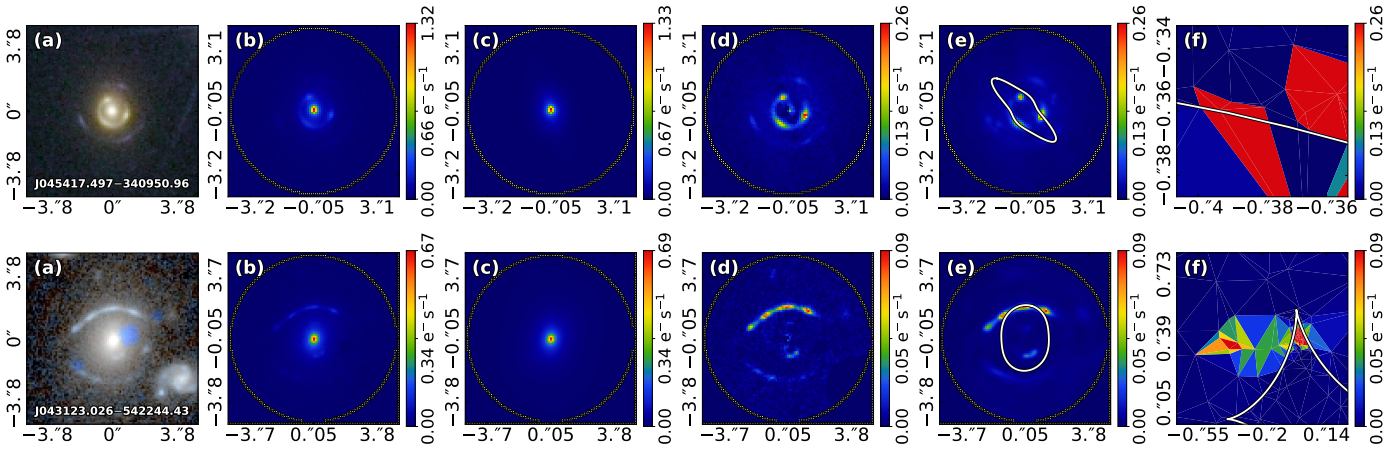


Fig. 6. Two outcomes of the Double Source Plane Lens (DSPL) classification. Panels follow the same layout as Fig. 3. The top row shows a genuine DSPL that inspectors correctly identified. Whilst the RGB image already provides strong visual evidence for multiple lensed sources, the poor lens-model fit resulting from the violation of the single-source-plane assumption provides an additional diagnostic that the system is a DSPL. The bottom row shows a grade A candidate receiving 4/5 (80%) DSPL votes. The additional blue feature south of (below) the lens may have motivated the DSPL classification, but its nature is uncertain: it could be associated with the main lensed source, a second lensed source, or an unrelated line-of-sight object. Visual agreement alone therefore does not establish the presence of two lensed sources at distinct redshifts.

The lower grade B rate does not arise mainly from more agreed modelling failures (9.6% versus 12.9%), but from more cases in which inspectors disagree (17.0% versus 37.6%). These no-consensus (NC) cases are included in the total from which the success rate is calculated, but they are neither confirmed successes nor confirmed failures. Instead, they form an ambiguous set of candidates for which inspectors' judgements differ too much for any classification to be assigned. We discuss NC cases in Sect. 6.6. Table 2 presents results for other thresholds.

Figure 3 shows three examples with SC-vote fractions of 100%, 75%, and 50%, respectively. The 14 additional lenses in Fig. C.1 provide a qualitative visual illustration of how SC, defined as confidence in the inferred Einstein radius, varies with inspector agreement. Models receiving at least 75% SC votes generally appear robust, whereas lower-agreement examples are more heterogeneous and more frequently exhibit features that could call the Einstein radius measurement into question, for example a counter-image that is not modelled correctly or a source reconstruction that fits light from a nearby galaxy missed by the segmentation process. However, by definition, even the results with thresholds as low as 50% are often of a quality for which many experts would consider the Einstein radius reliable. This illustrates that there will always be some ambiguity over whether a lens model is definitely considered successful.

A high SC-vote fraction does not imply that a model is free from limitations or suitable for every scientific application. Figure 4 shows two grade A examples with residual segmentation issues that are above the 75% consensus threshold for SC. In the top row, several nearby galaxies or stars are not masked and their light is mapped into the source reconstruction. In the bottom row, part of a genuine multiple image is incorrectly masked. In both cases the Einstein radius remains reliably constrained, but the products are less suitable for detailed source reconstruction or more complex mass modelling. These issues can be identified from the segmentation products and addressed through revised masks and remodelling.

6.2. UIL systems

UIL systems are cases where the visual evidence is insufficient for inspectors to confidently determine whether the object is a genuine strong lens, even after viewing the model diagnostics. At the adopted 75% threshold, Table 2 reports seven grade A UIL systems (0.1% of the grade A sample) and 123 grade B UIL systems (1.4%). Figure 5 shows two grade A systems with 100% UIL agreement. In the top row, the lens model does not reveal the corresponding counter-image to the north of the lens that would be expected for a convincing strong-lensing interpretation. In the bottom row, faint emission remains after subtraction of the foreground galaxy light, but its signal-to-noise ratio is too low to provide convincing evidence of lensing. These examples illustrate that an acceptable model fit alone does not establish the lensing nature of a candidate.

6.3. DSPL systems

DSPL systems contain multiple background sources at different redshifts lensed by the same foreground deflector. At the adopted 75% threshold, Table 2 reports 15 grade A DSPL systems (0.2% of the grade A sample) and four grade B DSPL systems ($< 0.1\%$). An important question is whether the inspectors can distinguish genuine DSPLs from conventional single-plane strong lenses. The top row of Fig. 6 shows a representative DSPL. The RGB image alone provides strong visual evidence that the system contains multiple lensed sources and was likely sufficient for most inspectors to identify it as a DSPL. However, because the lens model assumes a single source plane, it is unable to fit the system accurately, leading to obvious modelling residuals. This demonstrates that violations of the single-source-plane assumption can provide an additional diagnostic for identifying genuine DSPLs.

The bottom row of Fig. 6 shows a further grade A candidate receiving 4/5 (80%) DSPL votes. A second question is whether inspectors incorrectly identify single-plane strong lenses as DSPLs. To quantify this effect, a team of DSPL experts reinspected the nine objects in the 2990-candidate inspection that achieved at least 75% DSPL consensus. They concluded that four were not convincing DSPL candidates, illustrating that

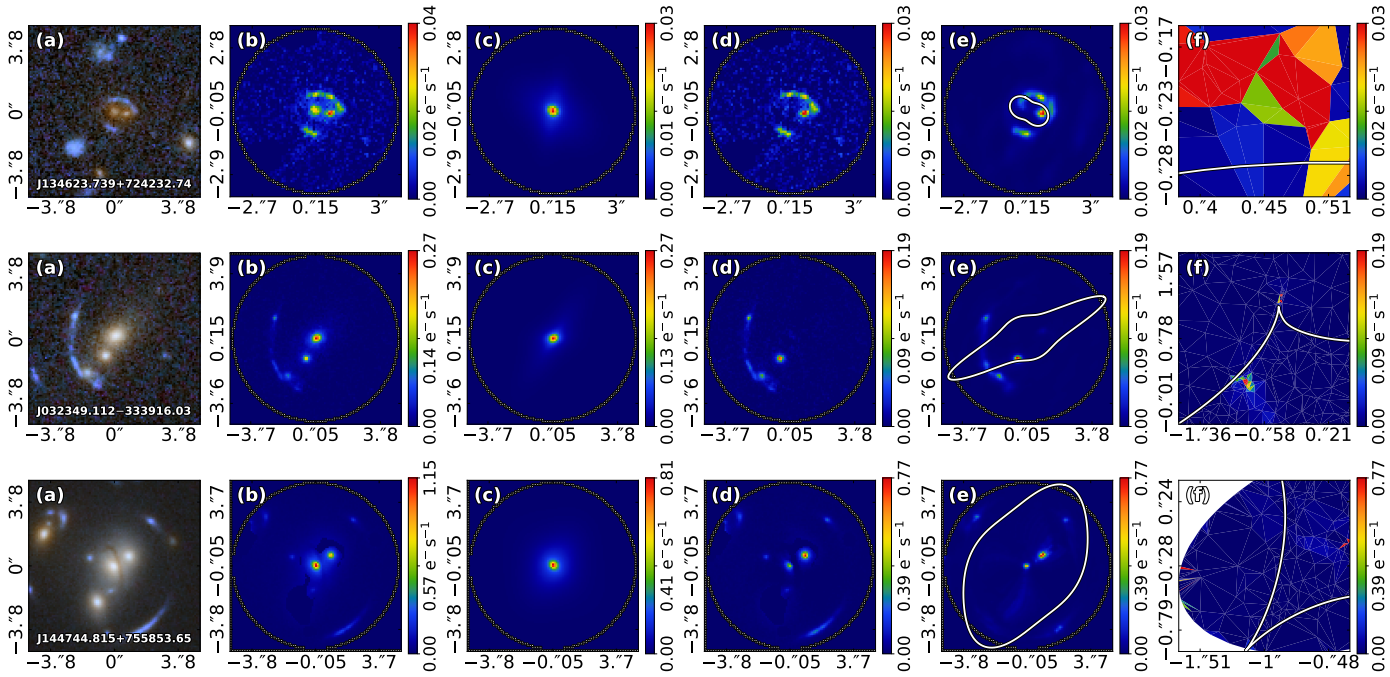


Fig. 7. Examples of grade A multi-galaxy lens (MGL) systems, each with 100% MGL agreement. Panels follow the same layout as Fig. 3. The top row shows a compact configuration of multiple foreground galaxies surrounded by arc-like emission, with an angular scale similar to that of single-galaxy lenses. The middle row shows multiple foreground galaxies with more extended arcs, whose lensed-source morphology would be difficult to reproduce with a single deflector. The bottom row shows a substantially larger MGL containing many foreground galaxies. Its scale and multiplicity are more characteristic of a group- or cluster-scale lens, conventionally associated in ΛCDM with a dark-matter halo mass above approximately $10^{14}\,M_{\odot}$.

Table 3. Secondary FL classifications from the 2990-object campaign, without a grade A restriction, within its 210 systems receiving FL at the adopted 75% primary-classification threshold. These are not the failure-mode fractions of the current grade A or grade B samples. Entries are percentages of this fixed FL sample; secondary agreement is measured among inspectors who voted FL on each system. The NC column gives the fraction for which inspectors did not reach the adopted agreement threshold on a secondary FL classification.

	Secondary FL classification			
Threshold	Segmentation	LensLight	SourceMass	NC
100%	11.4%	22.4%	3.3%	62.9%
75%	18.6%	31.4%	5.7%	44.3%
50%	29.0%	48.6%	15.7%	5.7%

visual inspection alone can leave the interpretation of additional source-like features ambiguous. However, these four objects represent only 0.13% of that sample and therefore have negligible impact on the overall classification statistics.

6.4. MGL systems

MGL systems contain more than one foreground lens galaxy within the Einstein radius. At the adopted 75% threshold, Table 2 reports 317 grade A MGL systems (5.2% of the grade A sample) and 385 grade B MGL systems (4.3%). Figure 7 shows that this category spans compact configurations of multiple foreground galaxies to more extended arc structures. Interestingly, the models in the first two rows appear qualitatively reasonable: their tangential critical curves suggest that the inferred Einstein radii may be approximately accurate, while their source reconstructions are focused and form smooth, galaxy-like morphologies. Nevertheless, these systems violate the single-deflector assumption of the current models and therefore require more detailed modelling before their inferred parameters can be used for scientific analysis. Dedicated multi-deflector modelling of the *Euclid* MGL population is presented by Euclid Collaboration: Wielders et al. (2026); we do not consider these systems further in this paper.

6.5. FL models

At the adopted 75% threshold, 580 grade A systems receive the FL classification (9.6% of the grade A sample). Secondary failure classifications were recorded only for the 2990-candidate inspection, so the examples and failure-mode breakdown below are drawn from that sample. The following examples separate failures using the secondary classifications adopted during visual inspection: FL-Segmentation, FL-LensLight, and FL-SourceMass. Table 3 gives the corresponding failure-mode consensus breakdown for the subset of systems for which at least 75% of inspectors selected FL in the primary classification. The percentages in this table are therefore conditional on a system being classified as FL.

FL-Segmentation failures make the likelihood inputs unreliable by excluding genuine lensed emission or retaining contaminating light. FL-LensLight, the most common agreed secondary FL classification, occurs when foreground lens light is not removed accurately enough for reliable source modelling. FL-SourceMass failures arise when the preprocessing and lens-light subtraction are sufficiently successful, but the inferred mass model or reconstructed source is not physically plausible. Figures 8 to 10 show representative examples.

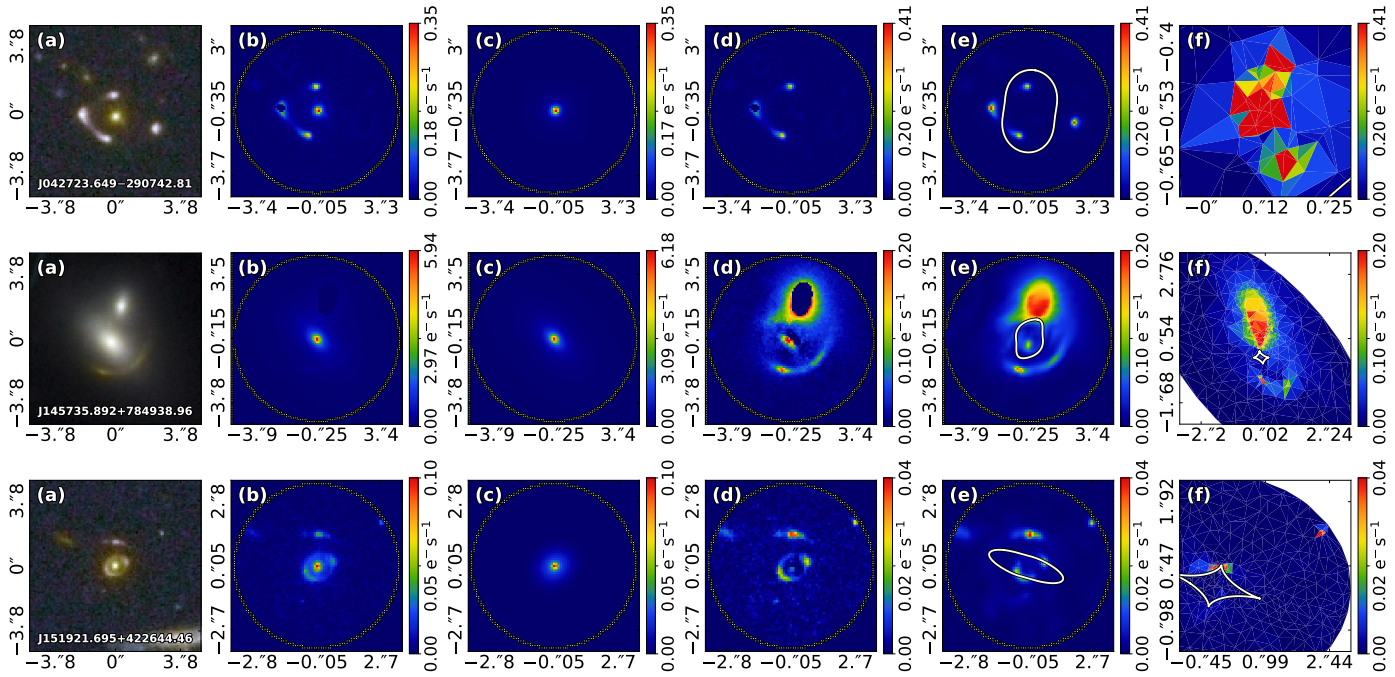


Fig. 8. Examples of Failure (FL) systems assigned the secondary FL-Segmentation classification. Panels follow the same layout as Fig. 3. In the top row, the segmentation incorrectly classifies one of the lensed multiple images as a line-of-sight galaxy, masking source emission required for a successful lens model. In the middle row, a contaminating galaxy to the south is identified but not fully masked, leaving residual emission that affects the source reconstruction. In the bottom row, nearby galaxies are missed entirely, including a galaxy to the south and additional objects near the edge of the mask, causing the model to fit contaminating light rather than only the lens and source emission.

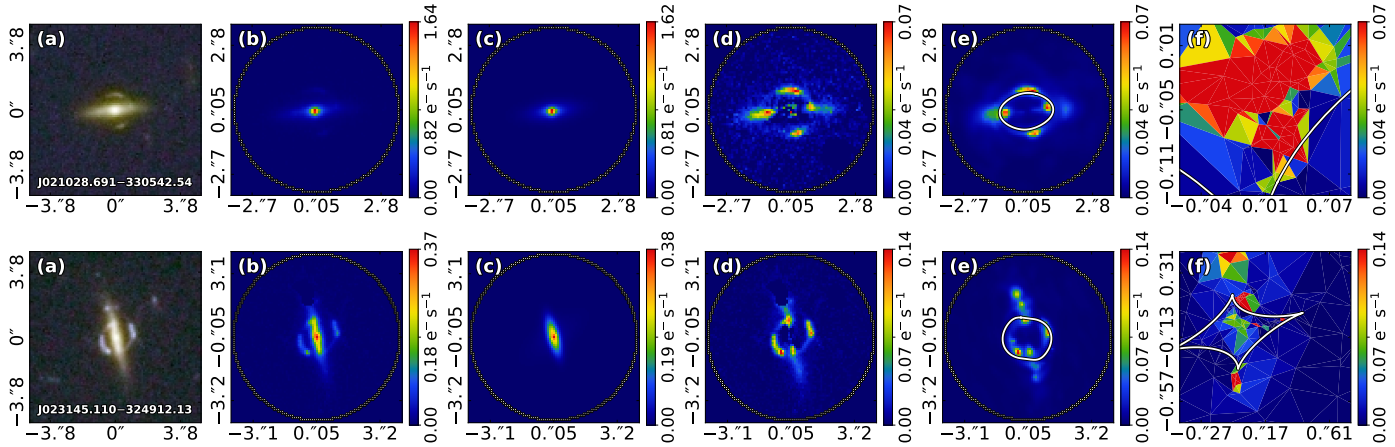


Fig. 9. Examples of Failure (FL) systems assigned the secondary FL-LensLight classification. Panels follow the same layout as Fig. 3. Residual foreground structure overlaps the lensed source emission in each system. In the top row, an edge-on disc lens galaxy leaves residuals at both ends of the galaxy, which overlap the lensed source emission. The bottom row shows a similar failure, but with stronger ripple-like residuals, plausibly associated with jets from an active galactic nucleus.

6.6. No-consensus classifications

A model is classified NC when no single classification reaches the 75% threshold. NC classifications are considerably more common for grade B candidates (37.6%) than for grade A (17.0%; Table 2), and grade B candidates also receive more individual votes for both modelling failure (FL) and uncertain lens status (UIL).

Figure 11 illustrates this ambiguity through examples of grade A and B candidates and their lens models. For many NC cases, the central difficulty is determining whether the candidate is genuinely a strong lens, rather than simply whether the model provides an adequate fit. A lens model may reproduce the observed emission without establishing its lensing origin, leading inspectors to disagree over both the nature of the candidate and the quality of the model. The lower grade B success rate therefore reflects greater uncertainty in lens identification, although some reduction in modelling performance cannot be ruled out.

6.7. Scientific results

Figure 12 shows the distribution of Einstein radii for the 7980 grade A and B systems classified as successfully modelled (SC) at the 75% consensus threshold. The distribution peaks near 0.″7, with a median of 0.″85, a 16th–84th percentile range of 0.″61–1.″29, and a tail extending beyond 2.″0, consistent with

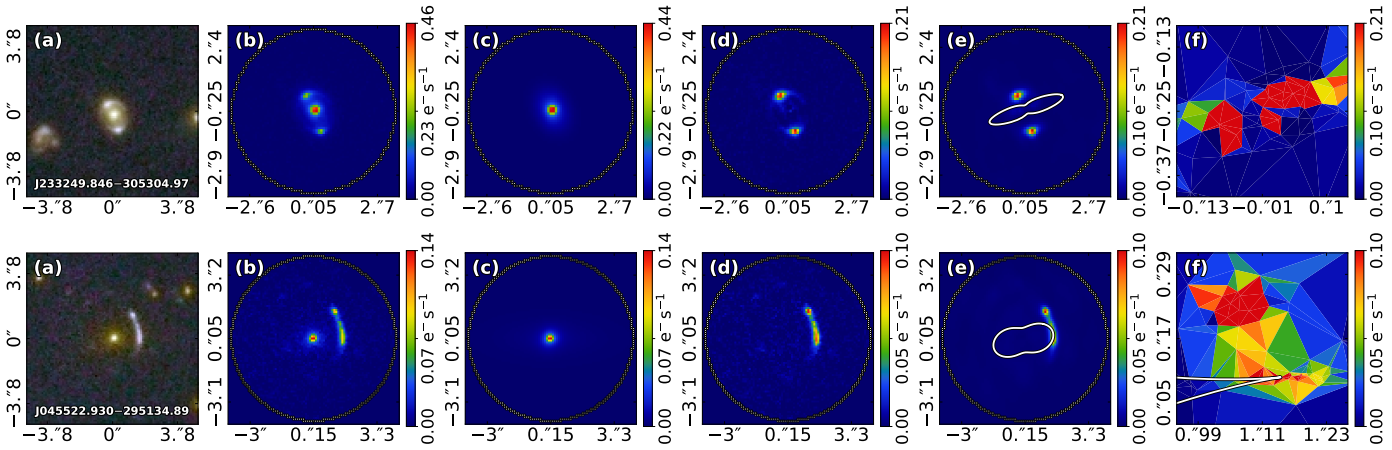


Fig. 10. Examples of Failure (FL) systems assigned the secondary FL-SourceMass classification. Panels follow the same layout as Fig. 3. These systems pass the initial preprocessing and lens-light subtraction stages but yield an implausible reconstructed source, lensed source model, or inferred mass model. In the top row, the mass model converges to an unphysically elliptical solution and predicts two faint central images that are not observed. In the bottom row, the model reconstructs the multiple images in the arcs to the right but fails to reconstruct their counter-image to the left because the incorrect mass model places the source outside the tangential caustic.

strong-lens population forecasts. We consider these point estimates suitable for characterising the sample but do not report individual parameter uncertainties, whose calibration against potential systematic errors in the modelling is deferred to future work. The quoted percentile ranges describe the spread across systems rather than measurement uncertainties.

We obtained lens-galaxy half-light radii from photometric fits that modelled both the lens and source light with Sérsic profiles, although potential biases from fitting-mask truncation remain unquantified. Figure 13 compares the lens-galaxy angular effective radius $\theta_{\rm eff}$ with the Einstein radius for 7976 successfully modelled systems (four SC systems lack a completed VIS Sérsic fit), finding a positive correlation (Spearman coefficient of 0.46). This is expected because more massive galaxies are generally larger and produce larger Einstein radii. The substantial scatter reflects variations in galaxy mass distributions, including dark matter, and differences in lens and source redshifts.

Figure 14 shows the distribution of total source magnifications μ, defined as the ratio of lensed to intrinsic source flux, measured in the $I_{\rm E}$ band for the same 7976 systems. The distribution peaks near $\mu \simeq 4$–6, with a median of 8.1 and a 16th–84th percentile range of 4.2–16.8. A high-magnification tail extends beyond $\mu \gtrsim 30$, with 92 systems exceeding $\mu = 60$ and 43 exceeding $\mu = 120$. Such extreme magnifications arise when sources lie close to lens caustics, where magnification becomes very large but remains finite for extended sources. These systems are particularly valuable for studying distant galaxies at enhanced sensitivity and effective angular resolution.

These magnifications assume an isothermal mass profile and may therefore be biased for lenses whose radial density slopes differ significantly from isothermal, particularly in the high-magnification tail. Although this can also bias inferred source sizes, simulations suggest that the reconstructed source morphology can remain accurate (Cao et al. 2022). Future work will quantify these systematic effects using power-law mass models with free radial slopes. Researchers requiring accurate magnifications or intrinsic source properties should account for this uncertainty, potentially by remodelling individual lenses with more flexible mass profiles.

6.8. ECLIPSE catalogue

All results presented in this work are publicly available through the ECLIPSE catalogue (ECLIPSE-A; Sect. 9). Alongside inspection classifications and inferred lens properties, including Einstein radii and source magnifications, we provide FITS images of deblended lens and source light, and source reconstructions across the VIS, NISP, and EXT bands (ECLIPSE-D), together with convergence, gravitational potential, and deflection-angle maps. Additional products include COOLEST-format lens models (Galan et al. 2023) and Witt–Wynne diagnostics (Witt 1996; Wynne & Schechter 2018; Schechter & Wynne 2019), which approximate the fitted caustics using elliptical potentials to rapidly predict image multiplicities, positions, and magnifications for lensed-transient searches (Schechter et al. 2026).[8] These approximations should be validated against the original lens models. The catalogue enables population-level studies and provides the community with the modelling products needed for independent analyses of individual strong lenses.

7. Discussion

7.1. Scaling up lens modelling

Our results demonstrate that strong-lens modelling can be scaled to survey-sized samples of more than ten thousand lenses, answering the question posed in the introduction. At the 75% consensus threshold, 4098 of 6073 grade A candidates (67.5%) are successfully modelled. The corresponding success rate for grade B candidates is 43.1%, with the drop due primarily to the subjectivity of classifying lower-confidence candidates, which leads to more cases without consensus (Sect. 6.6). Together, the two grades yield 7980 successful models. The full campaign modelled 15 072 candidates, over an order of magnitude more than any previous modelled strong-lens sample. The resulting ECLIPSE catalogue provides a foundation for population-level studies of galaxy formation, evolution, and cosmology, although precise scientific inferences will require further validation of measurement uncertainties and systematic errors in the modelling.

[8] Our implementation adapts `isit4or2or1` v1.0 (Schechter & Lu 2026).

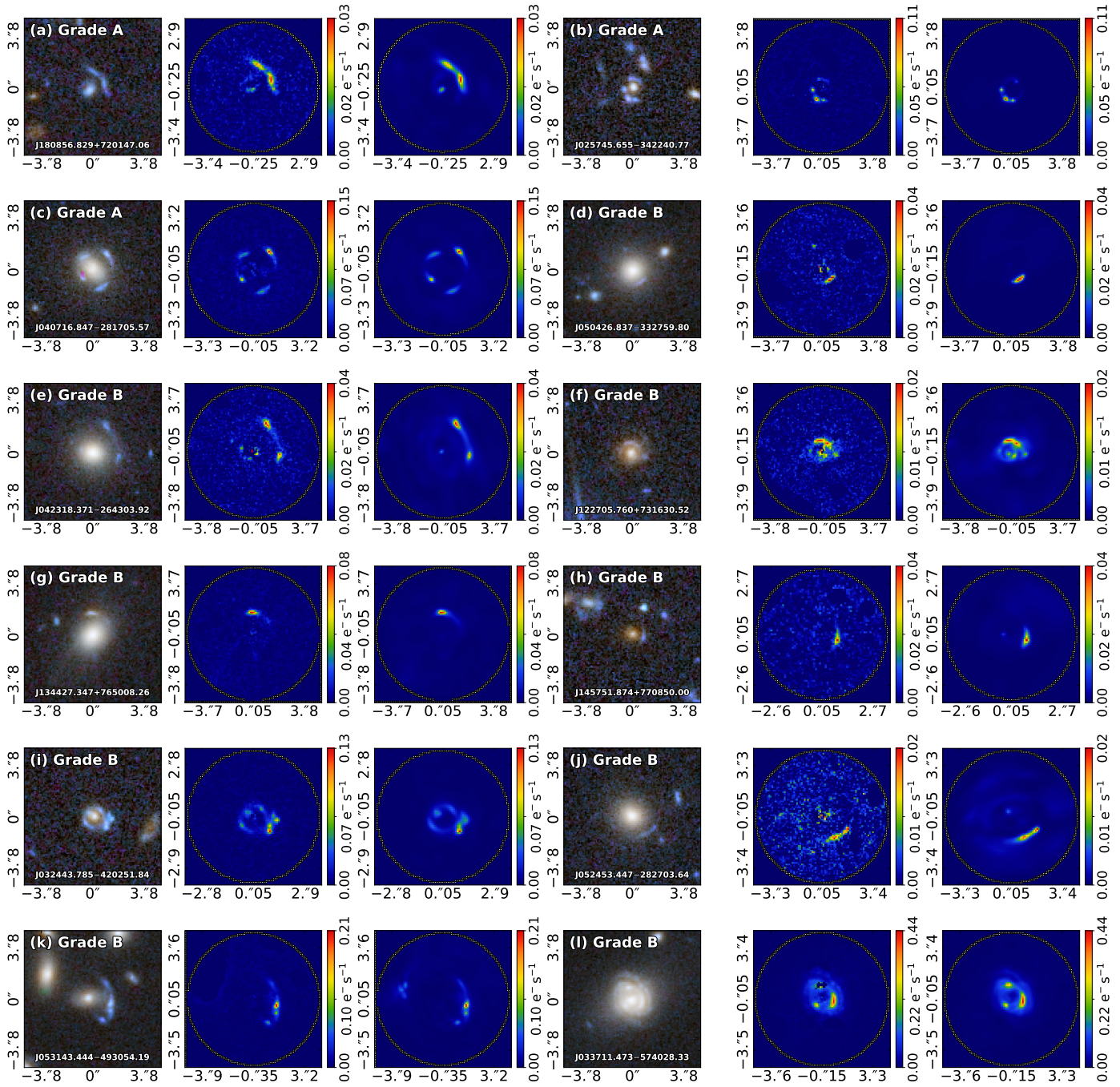


Fig. 11. Selected systems with no consensus (NC) classification at the 75% threshold. Reading left to right and top to bottom, the first three triplets show grade A candidates (a–c), and the remaining nine show grade B candidates (d–l). Each triplet displays the RGB image on the left, the VIS image after subtraction of the fitted foreground-galaxy light in the centre, and the lensed-source model image on the right, allowing a direct comparison of the residual emission and the model prediction. The examples illustrate the range of morphologies for which inspectors disagree, including uncertainty about whether the residual emission is genuinely lensed. They were selected for illustration and do not constitute a representative sample of either grade. The subtracted and model images share a colour scale within each triplet; this scale varies between systems.

We now consider the breakthroughs that have made scaling lens modelling to 15 072 systems possible. The first major breakthrough was not the lens modelling itself, but the machine-learning segmentation framework used in this work and presented by Euclid Collaboration: Vincken et al. (2026a). Previous automated lens modelling studies all relied on a human-intensive preprocessing stage where tasks such as masking the data and identifying contaminating galaxies were performed manually. In the Euclid Q1 modelling effort, the lead author of this work performed these preprocessing tasks manually for over 400 lenses, estimating that processing them all required approximately eight hours of repetitive GUI interaction, with inevitable human fatigue and inconsistency. Automating these preprocessing steps was therefore a critical requirement for scaling strong lens modelling to the sample sizes analysed in this work. Automating these steps also makes the masking procedure, and hence the modelling workflow, reproducible.

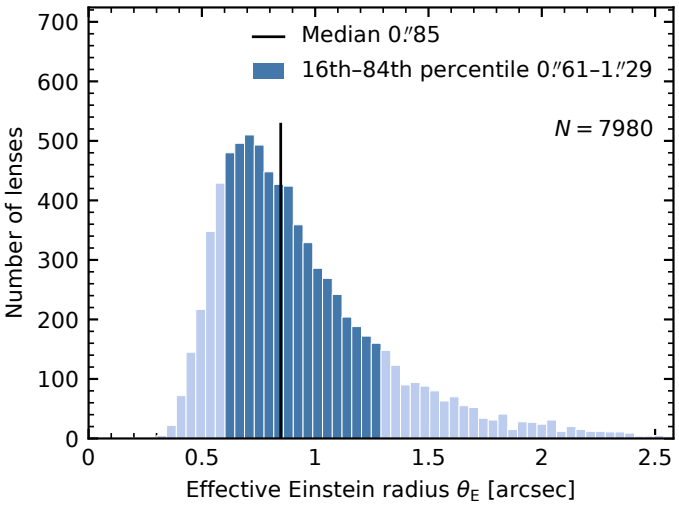


Fig. 12. Distribution of inferred effective Einstein radii θ_E for the systems classified as SC models at the 75% visual-inspection consensus threshold (N = 7980; grades A and B). The vertical line marks the median and the darker bars the 16th–84th percentile range. The histogram is truncated at the 99.5th percentile.

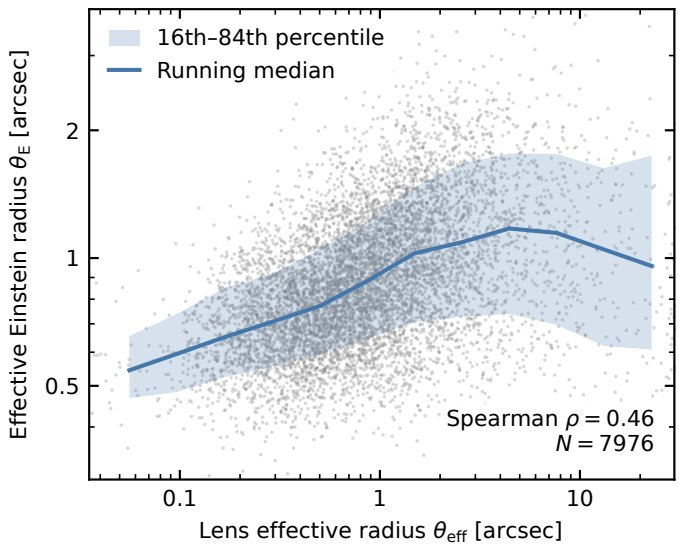


Fig. 13. Comparison between the foreground lens-galaxy angular effective radius θ_{eff} and the inferred Einstein radius θ_E for SC models at the 75% visual-inspection consensus threshold (N = 7976; grades A and B). Four of the 7980 SC systems lack a completed VIS Sérsic fit and are not shown here or in Fig. 14. The two quantities are positively correlated, indicating that larger lens galaxies generally produce larger Einstein radii, but with substantial scatter due to variations in galaxy mass structure and lens–source geometry. The solid line and shaded band show the running median and 16th–84th percentile range in log-spaced bins of the effective radius, and the annotation reports the Spearman rank correlation coefficient.

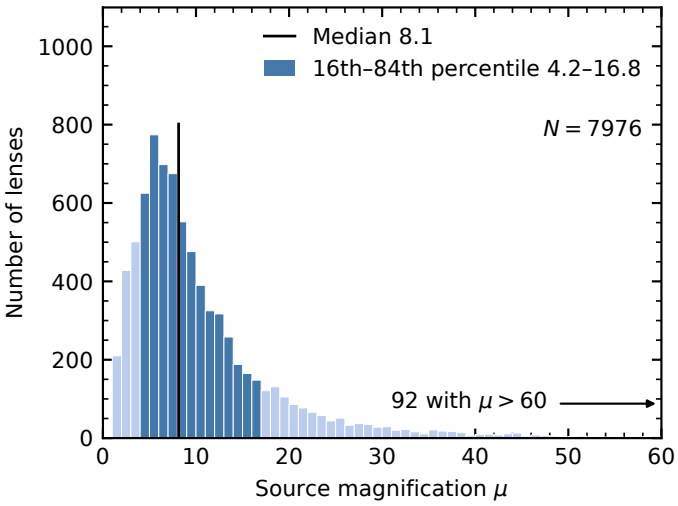


Fig. 14. Distribution of the total source magnification μ, the ratio of the lensed to the intrinsic source flux measured in the I_E band, for the SC models at the 75% visual-inspection consensus threshold (N = 7976; grades A and B). Four of the 7980 SC systems lack a completed VIS Sérsic fit and are not shown here or in Fig. 13. The vertical line marks the median and the darker bars the 16th–84th percentile range. The distribution is shown up to μ = 60; the annotation gives the number of systems above this value.

The lens modelling software used in this work, `PyAutoLens`, has undergone many improvements over the past decade that together enabled automated lens modelling at scale. The transition from Sérsic lens light models, as used by Etherington et al. (2022), to the MGE formalism (He et al. 2024) significantly reduced model failures caused by residuals from inadequate lens light subtraction degrading other components of the fit. In practical pipeline development, we observed fewer fits converging to local maxima as we moved from `MultiNest` (Feroz et al. 2009) to `Dynesty` (Speagle 2020) and finally `Nautilus`. Nightingale et al. (2025) also show that using an MGE source parameterisation in the first of the three sequential fits (Sect. 4.5) significantly simplifies the parameter space explored by the sampler: source size is represented through the linearly solved amplitudes of Gaussians with prescribed widths rather than fitted directly, reducing degeneracies with the lens mass model. In truth, automated strong lens modelling was not enabled by a single methodological breakthrough, but instead by many gradual and incremental improvements developed over more than ten years.

Machine-learning predictions offer a further route to improving model initialisation. Pearson et al. (2021) demonstrate the use of neural-network predictions and uncertainties as priors for `PyAutoLens`, while `LeMoN` (Euclid Collaboration: Busillo et al. 2026) provides rapid estimates of lens mass and light parameters that can inform subsequent modelling. Comparisons between `PyAutoLens` and `LeMoN` on subsets of the DR1 sample indicate that combining the approaches could improve the success rate. We did not incorporate machine-learning initialisation in the present analysis, prioritising a simple pipeline design for this initial scaling to 15 072 lenses. Broader comparisons of modelling methods are underway within the SL-SWG to identify systematic biases, following Galan et al. (2024).

Computational cost was not a barrier to this study. Modelling 15 072 strong-lens candidates required fewer than 250 000 CPU hours, relatively modest by modern high-performance computing (HPC) standards, with individual fits typically completing in under five hours. We used CPUs because they were readily available, while estimates from `PyAutoLens-Assistant` suggested they would also be more energy efficient for this workload. `PyAutoLens-Assistant` supported computational planning, monitoring, and aggregation of modelling results into catalogues shared with the SL-SWG, motivating further development of its natural-language interface for managing large modelling campaigns. `PyAutoLens` and other lens-modelling packages, including `herculens` (Galan et al. 2022), now support GPU acceleration, offering further potential speed-ups. These

modest computational requirements leave substantial scope for scaling to larger samples and more complex models.

Human inspection presents a greater challenge to scaling. At approximately 10 seconds per lens, four inspections of all 15 072 candidates require around 167 person-hours, or about 8 hours each for a team of 20 inspectors. Such an approach becomes impractical for samples exceeding 100 000 lenses. Automated goodness-of-fit statistics alone are insufficient: models can yield reliable Einstein radii despite imperfect lens-light subtraction (Etherington et al. 2022), while apparently good fits can contain unphysical source reconstructions. We therefore relied on multiple expert inspectors to assess the residuals, lens-light subtraction, critical curves, and source reconstructions. Developing reliable automated assessments is an important next step.

Agentic AI offers a potential solution to this inspection bottleneck. By assessing the imaging and model diagnostics together, an AI agent could identify reliable models, diagnose failures, and recommend or perform targeted remodelling, such as correcting faulty segmentation. Our visual-inspection campaign provides a data set against which such automated assessments can be developed and validated. Complementary machine-learning classifiers could identify double-source-plane lenses, multi-galaxy lenses, and other systems requiring specialised modelling. Together, these approaches could make the analysis of more than 100 000 lenses practical, with human inspectors focusing on ambiguous cases and validating automated decisions.

7.2. Fixing failures

Within the 2990-object inspection subset, 39 of the 210 failures were attributed to segmentation at the 75% secondary-classification threshold (Table 3). We anticipate that continued expansion of the `AstroVink-TREX` training data set will reduce these failures. The initial labelled data set comprised 377 Q1 systems (Euclid Collaboration: Vincken et al. 2026a); during this study, it was expanded first with a few hundred additional systems and then with 2990 DR1 lenses, producing the segmentation model applied to all 15 072 candidates. We observed improvements in segmentation performance as the training data set grew. The resulting models and visual-inspection assessments now provide a much larger pool from which to select reliable training examples and identify difficult cases for the next iteration. Further algorithmic improvements are also planned, including refinement of the loss function and contaminant separation, and extending the architecture to use multi-band information (Euclid Collaboration: Vincken et al. 2026a).

At the same threshold, 66 systems were classified as lens-light failures. These are predominantly associated with dust or asymmetric structure, including radial light profiles that rise in brightness away from the lens centre. Adding more concentric, symmetric Gaussian components, each with a monotonically decreasing radial brightness profile, cannot reproduce these features, so increasing the number of MGE sets is unlikely to resolve them. Such systems will likely require a different approach using a non-parametric lens-light model and, where necessary, explicit treatment of dust absorption. The matrix formalism incorporating lens light and dust extinction in Suyu et al. (2009, section 4, equation 13) provides a possible algebraic starting point for developing such a method. Separately, some lenses could benefit from the central point-like component used by H24, for example to represent a bright active galactic nucleus or other nuclear emission. Even without this component in our models, these systems were typically judged to yield reliable Einstein-radius measurements.

The 12 systems classified as source/mass failures suggest a further route to improvement through more robust sampling. Where these failures reflect convergence to an incorrect local maximum, increasing the number of live points in `Nautilus` could help locate the preferred solution. Combining sampling with machine-learning initialisation, for example using `LeMoN` (Euclid Collaboration: Busillo et al. 2026) as discussed above, could also improve convergence and recover failed models. Such approaches will also need to account for physical source–mass degeneracies, since source structure and regularisation assumptions in pixelised reconstructions can affect the inferred lens potential (Vernardos & Koopmans 2022).

7.3. Science with large strong lens samples

The ECLIPSE series models 15 072 grade A and B strong-lens candidates, providing the data and models needed for population-level studies and detailed investigations of individual systems. For successfully modelled lenses, Einstein radii, galaxy sizes and deblended photometry characterise the foreground galaxies, while magnifications and source reconstructions provide insights into the background population. Einstein radii are relatively robust to modelling choices (Etherington et al. 2022), while ECLIPSE-D evaluates the lens photometry for photometric-redshift estimation through comparison with MER. Future work using more flexible mass models will refine these measurements, particularly source magnifications and intrinsic sizes, which depend on the assumed radial mass profile (Sect. 6.7).

The *Euclid* strong-lens catalogue and lens models presented in this work provide a wealth of opportunities to study galaxy evolution and cosmology with strong gravitational lenses. For the lens galaxies themselves, these data establish strong lensing as a complementary tool to long-standing approaches such as stellar dynamics (e.g. Cappellari et al. 2011, 2013; Bundy et al. 2015) and stellar-population modelling (e.g. Bruzual & Charlot 2003; Thomas et al. 2005; Conroy 2013), providing the statistically significant samples needed to use lensing-inferred quantities as measurements of galaxy structure and evolution across a wide range of galaxy masses and redshifts. The Sérsic lens-light models released here will enable a census of lens-galaxy morphologies, including early-type, late-type, and S0 systems (e.g. Graham 2001; Graham & Driver 2005), while providing structural measurements such as Sérsic indices, effective radii, axis ratios, and luminosities. For both lenses and sources, these parameters provide familiar structural summaries for comparison with studies of unlensed galaxies; even a morphologically complex source can be characterised by a fitted effective radius and Sérsic index. Future bulge–disc decompositions could provide component sizes, luminosities and stellar masses (e.g. Simard et al. 2011; Mendel et al. 2014). Combined with lensing mass constraints, these would connect bulge and disc growth to the total mass distribution and star-formation quenching (e.g. Martig et al. 2009; Fang et al. 2013; Lang et al. 2014; Bluck et al. 2014, 2022).

When combined with SIE lens mass models and redshift information, these observables provide direct measurements of the projected total mass enclosed within the Einstein radius, a measure of the enclosed mass of lens galaxies that is not available for unlensed galaxies. This will enable extensions of classical galaxy scaling relations, such as the fundamental plane (Djorgovski & Davis 1987; Dressler et al. 1987) and Tully & Fisher

(1977) relation, in which lensing-inferred mass information is incorporated alongside photometric and, where available, dynamical quantities. Unlike many traditional galaxy-evolution probes, whose signal-to-noise ratio or diagnostic power often decreases rapidly with redshift, the lensing constraint is set primarily by the geometry and surface-brightness structure of the lensed images. Meaningful mass measurements can therefore often be extracted for higher-redshift lens galaxies in much the same way as for lower-redshift systems. The mass models released here thus provide a homogeneous view of the mass distributions of many thousands of massive galaxies over the redshift range $z \simeq 0.0$–2.0, opening a new route to studying the connection between galaxy structure, mass assembly, and evolution across cosmic time, complementary to local studies (e.g. Auger et al. 2010) that provide the essential $z \simeq 0$ baseline against which this evolution can be measured.

The strong-lens imaging modelled in this work contains substantially more information than the Einstein mass alone, encoded in the extended surface-brightness distribution of the lensed source. Fully exploiting this information will ultimately require more sophisticated lens models than those fitted here. Examples include power-law mass models (e.g. Koopmans et al. 2009; Shajib et al. 2021; Etherington et al. 2023), models that decompose the lens mass distribution into stellar and dark matter components (e.g. Sonnenfeld et al. 2013; Nightingale et al. 2019; Li et al. 2026b,a), and models that infer more detailed radial or angular structure in the mass distribution (e.g. Powell et al. 2022; Stacey et al. 2024). Incorporating complementary probes such as weak lensing or stellar dynamics pushes this further. We therefore anticipate that future lens-modelling studies will build on our work to exploit this information.

The models presented here also enable studies of the lensed source galaxies themselves. For every successfully modelled system, this work provides source magnification estimates and pixel-grid source reconstructions across the available imaging bands, enabling studies of intrinsic luminosities, morphologies, and colours after correcting for the lensing distortion. There are already many examples of galaxy-scale strong lenses being used to study background galaxies in detail (e.g. Dye et al. 2014; Swinbank et al. 2015; Rizzo et al. 2020; Amvrosiadis et al. 2025), but such analyses have often been limited by sample size: researchers have not generally been able to select, from large parent samples, the particular magnified sources best matched to a given science case. The scale of the *Euclid* sample changes this. On cluster scales, large magnifications have enabled major progress in the study of galaxies at redshifts greater than 10 (e.g. Coe et al. 2013; Atek et al. 2015; Lotz et al. 2017). Galaxy-scale lenses offer comparatively simple mass models for source reconstruction, while magnification improves the effective spatial resolution of source structure for a given observation (e.g. Rizzo et al. 2020). Their compact angular extent also allows an individual lens system, including its multiple images, to fit within a single integral-field-unit field of view for suitably chosen targets and instruments. The catalogue therefore provides a large, selectable sample of magnified galaxies for future studies of resolved galaxy structure, stellar populations, and kinematics, with the richest constraints expected at redshifts $z \simeq 0.5$–3.0 and smaller subsamples extending to $z \simeq 8.0$.

One avenue for future work is to select lenses suited to specific science cases and obtain targeted follow-up observations. For dark-matter studies, such samples can constrain the abundance of low-mass haloes (e.g. Vegetti et al. 2018, 2024), with sensitivity estimates guiding the selection of targets for deeper or higher-resolution imaging (e.g. O'Riordan et al. 2023). These analyses must also account for angular structure in the lens mass distribution, which can mimic substructure signals (e.g. O'Riordan & Vegetti 2024; Lange et al. 2025). For cosmography, the large parent sample, combined with detailed modelling and stellar-kinematic follow-up of selected lenses, could help constrain the diversity of galaxy mass profiles and the associated mass-sheet degeneracy (Schneider & Sluse 2013, 2014; Birrer et al. 2020). Accounting for this degeneracy is essential both for time-delay cosmography and for cosmological inference from double-source-plane lenses (Schneider 2014).

We anticipate high-quality photometric redshifts for most lens galaxies, which are preferentially bright and massive (ECLIPSE-D). Spectroscopic follow-up will provide complementary information: the 4MOST Strong Lensing Spectroscopic Legacy Survey (4SLSLS) aims to obtain approximately 10 000 source redshifts for *Euclid* and LSST lens candidates (Collett et al. 2023). Spectroscopic completeness may therefore be achievable for selected samples targeting cosmology or dark matter, but is unlikely for the full population of more than 100 000 lenses. Exploiting that population will require improved photometric redshifts and methods that propagate redshift uncertainties into lensing inference, including joint analyses that account for the source population and lens selection function (e.g. Sonnenfeld 2022a,b).

8. Conclusions

We have presented automated lens modelling of 15 072 strong-lens candidates from Euclid Data Release 1 (DR1), over an order of magnitude more than any previous modelled strong-lens sample. Using `PyAutoLens`, we combined automated machine-learning preprocessing, MGE lens-light subtraction, an isothermal ellipsoid mass model with external shear, and parametric and pixelised source reconstructions. The resulting models were visually assessed by more than 20 expert inspectors from the SL-SWG. Our main conclusions are:

- *Modelling success rates:* At 75% expert agreement, 4098 of 6073 grade A (secure) candidates (67.5%) and 3882 of 8999 grade B (probable) candidates (43.1%) are successfully modelled, yielding a total of 7980 successful models.
- *Grade B uncertainty:* The lower grade B success rate primarily reflects greater disagreement between inspectors (37.6% without consensus, compared with 17.0% for grade A), rather than a comparable increase in agreed modelling failures (12.9% versus 9.6%). We attribute much of this disagreement to uncertainty over whether grade B candidates are genuine lenses.
- *Modelling failures:* For a subset of 2990 candidates, we analysed 210 consensus modelling failures. The most common identified cause is inaccurate lens-light subtraction (31.4%), followed by segmentation errors (18.6%) and source-reconstruction or mass-model failures (5.7%), with the remaining 44.3% lacking consensus on the failure mode.
- *Lens properties:* Successfully modelled systems have a median Einstein radius of 0.″85, with a 16th–84th percentile range of 0.″61–1.″29. We consider these point estimates suitable for characterising the population, while calibration of individual parameter uncertainties and systematic errors in the modelling is left to future work.
- *Public catalogue:* We release the successful lens models and their inferred properties through the ECLIPSE catalogue,[9] alongside masks, segmentation maps, deblended

[9] `https://euclid-eclipse-lenses.org`

multi-wavelength imaging, source reconstructions, and lens mass maps. These products enable both population-level studies and detailed investigations of individual systems.

Our results demonstrate that automated strong-lens modelling can scale to the thousands of systems being discovered by *Euclid*. The ECLIPSE catalogue provides a foundation for studying galaxy mass distributions, the connection between baryons and dark matter, galaxy evolution, and cosmology. The approach also provides a basis for automated modelling of strong lenses from surveys with *Roman*, the China Space Station Telescope (CSST), and the Vera C. Rubin Observatory. Extending this approach to future *Euclid* releases, alongside improvements in automated model assessment and uncertainty calibration, will establish strong lensing as an increasingly powerful statistical probe of galaxy formation and cosmology.

9. Data availability

The lens catalogue, lens models, photometric redshifts, and stellar population properties are available on Zenodo at `https://doi.org/10.5281/zenodo.19654904`. For every successfully modelled lens, the release includes the inferred lens-model parameters and derived quantities, together with the masks, segmentation maps, deblended multi-wavelength imaging, source reconstructions, and lens mass maps described in this work. The catalogue can also be browsed interactively at `https://euclid-eclipse-lenses.org`. The *Euclid* DR1 data, including all the catalogues and imaging used in this work, are available to download from `https://eas.esac.esa.int/sas/` and are described at `https://www.cosmos.esa.int/web/euclid/data-release-dr1`.

Software

Acknowledgements. JWN is supported by an STFC/UKRI Ernest Rutherford Fellowship, Project Reference: ST/X003086/1, and acknowledges travel support provided by Euclid:UK through STFC grant APP91126. NL is supported through a graduate studentship from the UKRI STFC and the University of Portsmouth, and acknowledges travel support provided by Euclid:UK through STFC grant APP91126 and by STFC for UK participation in the Rubin LSST through grant ST/X001334/1. This work has received funding from the European Research Council (ERC) under the European Union's Horizon 2020 research and innovation programme (LensEra: grant agreement No. 945536). TEC is funded by the Royal Society through a University Research Fellowship. PH is funded by the Royal Society (RF/ERE/210033) and acknowledges travel support provided by Euclid:UK through STFC grant APP91126. AN gratefully acknowledges the support of the Belgian Federal Science Policy Office (BELSPO) for the provision of financial support in the framework of the PRODEX Programme of the European Space Agency (ESA) under contract number 4000143347. CJS acknowledges funding from the NASA Euclid General Investigator Program Grant No. 80NSSC25K7735. WJRE acknowledges the support by the Italian Ministry of University and Research (grant FIS2023-01611, CUP C53C25000300001). AS acknowledges support from the National Key R&D Program of China (No. 2023YFA1607800, 2023YFA1607802), and from the Yangyang Development Fund. AG acknowledges support by the SNSF through PostDoc Mobility Return grant P5R5-2_235360. QH was supported by the Dutch Research Council (NWO) through the grant Open Competitie ENW M21-1. DJ acknowledges support by the First Rand Foundation, South Africa, and the Centre National de la Recherche Scientifique of France. SKL acknowledges the generous support from the Croucher Foundation through the Croucher Postdoctoral Fellowship. PB acknowledges financial support from the Italian Space Agency (ASI) through contract "Euclid - Phase E", and INAF Grants "The Big-Data era of cluster lensing" and "Probing Dark Matter and Galaxy Formation in Galaxy Clusters through Strong Gravitational Lensing". JAAB's research was supported by an appointment to the NASA Postdoctoral Program at the NASA Jet Propulsion Laboratory administered by Oak Ridge Associated Universities under contract with NASA. Part of this research was carried out at the Jet Propulsion Laboratory, California Institute of Technology, under a contract with the National Aeronautics and Space Administration (80NM0018D0004). SHV is supported by the ELSA project. 'ELSA: Euclid Legacy Science Advanced analysis tools' (Grant Agreement no. 101135203) is funded by the European Union. Views and opinions expressed are however those of the author(s) only and do not necessarily reflect those of the European Union or Innovate UK. Neither the European Union nor the granting authority can be held responsible for them. UK participation is funded through the UK Horizon guarantee scheme under Innovate UK grant 10093177. Numerical computations were carried out on the SCIAMA High Performance Compute (HPC) cluster, which is supported by the ICG, SEPNet, and the University of Portsmouth. This work used IRIS computing resources funded by the Science and Technology Facilities Council. This research makes use of ESA Datalabs (`datalabs.esa.int`), an initiative by ESA's Data Science and Archives Division in the Science and Operations Department, Directorate of Science. This work has made use of the *Euclid* Data Release 1 (DR1) from the European Space Agency (ESA) mission *Euclid*, available at `https://www.cosmos.esa.int/web/euclid/data-release-dr1`. The Euclid Consortium acknowledges the European Space Agency and a number of agencies and institutes that have supported the development of *Euclid*, in particular the Agenzia Spaziale Italiana, the Austrian Forschungsförderungsgesellschaft funded through BMIMI, the Belgian Science Policy, the Canadian Euclid Consortium, the Deutsches Zentrum für Luft- und Raumfahrt, the DTU Space and the Niels Bohr Institute in Denmark, the French Centre National d'Etudes Spatiales, the Fundação para a Ciência e a Tecnologia, the Hungarian Academy of Sciences, the Ministerio de Ciencia, Innovación y Universidades, the National Aeronautics and Space Administration, the National Astronomical Observatory of Japan, the Netherlandse Onderzoekschool Voor Astronomie, the Norwegian Space Agency, the Research Council of Finland, the Romanian Space Agency, the Swiss Space Office (SSO) at the State Secretariat for Education, Research, and Innovation (SERI), and the United Kingdom Space Agency. A complete and detailed list is available on the *Euclid* web site (`www.euclid-ec.org/consortium/community/`).

References

Acevedo Barroso, J. A., O'Riordan, C. M., Clément, B., et al. 2025, A&A, 697, A14
Amvrosiadis, A., Lange, S., Nightingale, J. W., et al. 2025, MNRAS, 537, 1163
Atek, H., Richard, J., Kneib, J. P., et al. 2015, ApJ, 800, 18
Auger, M. W., Treu, T., Bolton, A. S., et al. 2010, ApJ, 724, 511
Birrer, S. & Amara, A. 2018, Physics of the Dark Universe, 22, 189
Birrer, S., Refregier, A., & Amara, A. 2018, ApJL, 852, L14
Birrer, S., Shajib, A. J., Galan, A., et al. 2020, A&A, 643, A165
Birrer, S., Welschen, C., Amara, A., & Refregier, A. 2017, JCAP, 04, 049
Bluck, A. F. L., Maiolino, R., Brownson, S., et al. 2022, A&A, 659, A160
Bluck, A. F. L., Mendel, J. T., Ellison, S. L., et al. 2014, MNRAS, 441, 599
Bolton, A. S., Burles, S., Koopmans, L. V. E., et al. 2008, ApJ, 682, 964
Bro, R. & De Jong, S. 1997, Journal of Chemometrics, 11, 393
Brownstein, J. R., Bolton, A. S., Schlegel, D. J., et al. 2012, ApJ, 744, 41
Bruzual, G. & Charlot, S. 2003, MNRAS, 344, 1000
Bundy, K., Bershady, M. A., Law, D. R., et al. 2015, ApJ, 798, 7
Cao, X., Li, R., Nightingale, J. W., et al. 2022, Research in Astronomy and Astrophysics, 22, 025014
Cappellari, M. 2002, MNRAS, 333, 400
Cappellari, M., Emsellem, E., Krajnović, D., et al. 2011, MNRAS, 413, 813
Cappellari, M., McDermid, R. M., Alatalo, K., et al. 2013, MNRAS, 432, 1862
Coe, D., Zitrin, A., Carrasco, M., et al. 2013, ApJ, 762, 32
Collett, T. E. 2015, ApJ, 811, 20
Collett, T. E. & Auger, M. W. 2014, MNRAS, 443, 969
Collett, T. E., Sonnenfeld, A., Frohmaier, C., et al. 2023, The Messenger, 190, 49
Conroy, C. 2013, ARA&A, 51, 393
Djorgovski, S. & Davis, M. 1987, ApJ, 313, 59
Dressler, A., Lynden-Bell, D., Burstein, D., et al. 1987, ApJ, 313, 42
Dye, S., Furlanetto, C., Dunne, L., et al. 2018, MNRAS, 476, 4383
Dye, S., Negrello, M., Hopwood, R., et al. 2014, MNRAS, 440, 2013
Ertl, S., Schuldt, S., Suyu, S. H., et al. 2023, A&A, 672, A2
Etherington, A., Nightingale, J. W., Massey, R., et al. 2022, MNRAS, 517, 3275
Etherington, A., Nightingale, J. W., Massey, R., et al. 2023, MNRAS, 521, 6005
Etherington, A., Nightingale, J. W., Massey, R., et al. 2024, MNRAS, 531, 3684
Euclid Collaboration: Busillo, V., Tortora, C., Metcalf, R. B., et al. 2026, A&A, 711, A31
Euclid Collaboration: Cropper, M., Al-Bahlawan, A., Amiaux, J., et al. 2025, A&A, 697, A2
Euclid Collaboration: Ecker, L. R., Fabricius, M., Seitz, S., et al. 2026, A&A [arXiv:2603.28580], submitted
Euclid Collaboration: Holloway, P., Verma, A., Walmsley, M., et al. 2026a, A&A, 711, A30
Euclid Collaboration: Holloway, P. et al. 2026b, A&A, in preparation
Euclid Collaboration: Jahnke, K., Gillard, W., Schirmer, M., et al. 2025, A&A, 697, A3

Euclid Collaboration: Li, T., Collett, T. E., Walmsley, M., et al. 2026, A&A, 711, A29
Euclid Collaboration: Lines, N. et al. 2026a, A&A, in preparation
Euclid Collaboration: Lines, N. E. P., Collett, T. E., Walmsley, M., et al. 2026b, A&A, 711, A28
Euclid Collaboration: McCracken, H. et al. 2026a, A&A, in preparation
Euclid Collaboration: McCracken, H. J., Benson, K., Dolding, C., et al. 2026b, A&A, 711, A2
Euclid Collaboration: Mellier, Y., Abdurro'uf, Acevedo Barroso, J., et al. 2025, A&A, 697, A1
Euclid Collaboration: Nersesian et al. 2026, A&A, in preparation
Euclid Collaboration: Rojas, K., Collett, T. E., Acevedo Barroso, J. A., et al. 2026, A&A, 711, A27
Euclid Collaboration: Romelli, E., Kümmel, M., Dole, H., et al. 2026, A&A, 711, A4
Euclid Collaboration: Scaramella, R., Amiaux, J., Mellier, Y., et al. 2022, A&A, 662, A112
Euclid Collaboration: Vincken, S. H., Lines, N. E. P., Nightingale, J., et al. 2026a, in preparation
Euclid Collaboration: Vincken, S. H., Rojas, K., Melchior, M., et al. 2026b, arXiv e-prints [arXiv:2604.21977]
Euclid Collaboration: Walmsley, M., Holloway, P., Lines, N. E. P., et al. 2026, A&A, 711, A26
Euclid Collaboration: Wielders, N. J. H. R., Nightingale, J. W., et al. 2026, A&A, in preparation
Euclid Data Release 1. 2026, https://doi.org/10.57780/esa-d079c51
Fang, J. J., Faber, S. M., Koo, D. C., & Dekel, A. 2013, ApJ, 776, 63
Feroz, F., Hobson, M. P., & Bridges, M. 2009, MNRAS, 398, 1601
Ferrami, G. & Wyithe, J. S. B. 2024, MNRAS, 532, 1832
Fleury, P., Johnson, D., Duboscq, T., Hogg, N. B., & Larena, J. 2026, JCAP, 09, 101
Galan, A., Van de Vyvere, L., Gomer, M. R., Vernardos, G., & Sluse, D. 2023, Journal of Open Source Software, 8, 5567
Galan, A., Vernardos, G., Minor, Q., et al. 2024, A&A, 692, A87
Galan, A., Vernardos, G., Peel, A., Courbin, F., & Starck, J.-L. 2022, A&A, 668, 24
Gavazzi, R., Marshall, P. J., Treu, T., & Sonnenfeld, A. 2014, ApJ, 785, 144
Graham, A. W. 2001, AJ, 121, 820
Graham, A. W. & Driver, S. P. 2005, PASA, 22, 118
He, Q., Nightingale, J. W., Amvrosiadis, A., et al. 2024, MNRAS, 532, 2441
He, Q., Robertson, A., Nightingale, J. W., et al. 2025, ApJL, 991, L53
Hogg, N. B., Fleury, P., Larena, J., & Martinelli, M. 2023, MNRAS, 520, 5982
Hogg, N. B., Johnson, D. P., Shajib, A. J., & Larena, J. 2026, The Open Journal of Astrophysics, 9, 164832
Holloway, P., Verma, A., Marshall, P. J., More, A., & Tecza, M. 2023, MNRAS, 525, 2341
Kochanek, C. S. 2006, in Saas-Fee Advanced Course, Vol. 33, Gravitational Lensing: Strong, Weak and Micro (Springer Berlin Heidelberg), 91–268
Koopmans, L. V., Bolton, A., Treu, T., et al. 2009, ApJ, 703, L51
Krawczyk, C. 2025, JaxNNLS: Non-negative least-squares solver in JAX, Software, https://github.com/CKrawczyk/JaxNNLS
Lang, P., Wuyts, S., Somerville, R. S., et al. 2014, ApJ, 788, 11
Lange, J. U. 2023, MNRAS, 525, 3181
Lange, S. C., Amvrosiadis, A., Nightingale, J. W., et al. 2025, MNRAS, 539, 704
Li, T., Collett, T. E., Krawczyk, C. M., Enzi, W. J. R., & Galan, A. 2026a, arXiv e-prints [arXiv:2607.08576]
Li, T., Collett, T. E., Krawczyk, C. M., et al. 2026b, MNRAS, 548, stag683
Lotz, J. M., Koekemoer, A., Coe, D., et al. 2017, ApJ, 837, 97
Maresca, J., Dye, S., & Li, N. 2021, MNRAS, 503, 2229
Martig, M., Bournaud, F., Teyssier, R., & Dekel, A. 2009, ApJ, 707, 250
Mendel, J. T., Simard, L., Palmer, M., Ellison, S. L., & Patton, D. R. 2014, ApJS, 210, 3
Nightingale, J., Hayes, R., Kelly, A., et al. 2021, J. Open Source Softw., 6, 2825
Nightingale, J. W., Dye, S., & Massey, R. J. 2018, MNRAS, 478, 4738
Nightingale, J. W., He, Q., Cao, X., et al. 2024, MNRAS, 527, 10480
Nightingale, J. W., Mahler, G., McCleary, J., et al. 2025, MNRAS, 543, 203
Nightingale, J. W., Massey, R. J., Harvey, D. R., et al. 2019, MNRAS, 489, 2049
Oguri, M., Rusu, C. E., & Falco, E. E. 2014, MNRAS, 439, 2494
O'Riordan, C. M., Despali, G., Vegetti, S., Lovell, M. R., & Moliné, Á. 2023, MNRAS, 521, 2342
O'Riordan, C. M., Oldham, L. J., Nersesian, A., et al. 2025, A&A, 694, A145
O'Riordan, C. M. & Vegetti, S. 2024, MNRAS, 528, 1757
Pearson, J., Maresca, J., Li, N., & Dye, S. 2021, MNRAS, 505, 4362
Powell, D. M., Vegetti, S., McKean, J. P., et al. 2022, MNRAS, 516, 1808
Rizzo, F., Vegetti, S., Powell, D., et al. 2020, Nat, 584, 201
Sahu, N., Shajib, A. J., Tran, K.-V., et al. 2025, ApJ, 991, 72
Schechter, P. & Lu, M. Z. 2026, Source code to determine whether a supernova is quadruply, doubly or singly lensed, Zenodo, version isit4or2or1.v1.0
Schechter, P. L., Lu, M. Z., & Hernández, C. 2026, arXiv e-prints [arXiv:2605.11090]
Schechter, P. L. & Wynne, R. A. 2019, ApJ, 876, 9
Schmidt, T., Treu, T., Birrer, S., et al. 2023, MNRAS, 518, 1260
Schneider, P. 2014, A&A, 568, L2
Schneider, P. & Sluse, D. 2013, A&A, 559, A37
Schneider, P. & Sluse, D. 2014, A&A, 564, A103
Schuldt, S., Suyu, S. H., Cañameras, R., et al. 2023, A&A, 673, A33
Shajib, A. J., Birrer, S., Treu, T., et al. 2019, MNRAS, 483, 5649
Shajib, A. J., Nihal, N. S., Tan, C. Y., et al. 2025, ApJ, 992, 40
Shajib, A. J., Treu, T., Birrer, S., & Sonnenfeld, A. 2021, MNRAS, 503, 2380
Shajib, A. J., Vernardos, G., Collett, T. E., et al. 2024, Space Science Reviews, 220, 87
Shu, Y., Bolton, A. S., Kochanek, C. S., et al. 2016, ApJ, 824, 86
Simard, L., Mendel, J. T., Patton, D. R., Ellison, S. L., & McConnachie, A. W. 2011, ApJS, 196, 11
Sonnenfeld, A. 2021, A&A, 656, A153
Sonnenfeld, A. 2022a, A&A, 659, A132
Sonnenfeld, A. 2022b, A&A, 659, A133
Sonnenfeld, A. & Cautun, M. 2021, A&A, 651, A18
Sonnenfeld, A., Gavazzi, R., Suyu, S. H., Treu, T., & Marshall, P. J. 2013, ApJ, 777, 97
Sonnenfeld, A., Treu, T., Marshall, P. J., et al. 2015, ApJ, 800, 94
Speagle, J. S. 2020, MNRAS, 493, 3132
Stacey, H. R., Powell, D. M., Vegetti, S., et al. 2024, A&A, 688, A110
Suyu, S. H., Bonvin, V., Courbin, F., et al. 2017, MNRAS, 468, 2590
Suyu, S. H., Marshall, P. J., Blandford, R. D., et al. 2009, ApJ, 691, 277
Suyu, S. H., Marshall, P. J., Hobson, M. P., & Blandford, R. D. 2006, MNRAS, 371, 983
Swinbank, A. M., Dye, S., Nightingale, J. W., et al. 2015, ApJ, 806, L17
Tessore, N. & Metcalf, R. B. 2015, A&A, 580, A79
Thomas, D., Maraston, C., Bender, R., & Mendes de Oliveira, C. 2005, ApJ, 621, 673
Tracy, K. & Manchester, Z. 2024, On the Differentiability of the Primal-Dual Interior-Point Method, arXiv:2406.11749
Tran, K.-V. H., Harshan, A., Glazebrook, K., et al. 2022, AJ, 164, 148
Treu, T. 2010, ARA&A, 48, 87
Treu, T., Dutton, A. A., Auger, M. W., et al. 2011, MNRAS, 417, 1601
Tully, R. B. & Fisher, J. R. 1977, A&A, 54, 661
Vegetti, S., Birrer, S., Despali, G., et al. 2024, Space Sci. Rev., 220, 58
Vegetti, S., Despali, G., Lovell, M. R., & Enzi, W. 2018, MNRAS, 481, 3661
Vegetti, S. & Koopmans, L. V. 2009, MNRAS, 392, 945
Vegetti, S., Koopmans, L. V. E., Auger, M. W., Treu, T., & Bolton, A. S. 2014, MNRAS, 442, 2017
Vernardos, G. & Koopmans, L. V. E. 2022, MNRAS, 516, 1347
Warren, S. & Dye, S. 2003, ApJ, 590, 673
Witt, H. J. 1996, ApJ, 472, L1
Wong, K. C., Suyu, S. H., Chen, G. C.-F., et al. 2020, MNRAS, 498, 1420
Wynne, R. A. & Schechter, P. L. 2018, arXiv e-prints [arXiv:1808.06151]

Authors and affiliations

Euclid Collaboration: J. W. Nightingale⋆[1], S. H. Vincken[2], L. R. Ecker[3,4,5], A. Nersesian[6,7], D. J. Bowden[8], C. M. O'Riordan[5], N. E. P. Lines[9], T. E. Collett[9], G. Despali[10,11,12], S. Schuldt[13,14,15], F. Courbin[16,17,18], R. B. Metcalf[10,11], A. Verma[8], A. Angress[19,20], W. J. R. Enzi[9,21], K. Finner[22], P. Fleury[23], M. Fogliardi[24,11], A. Galan[25], R. Gavazzi[26,27], Q. He[28], N. B. Hogg[29,30], P. Holloway[9], D. P. Johnson[23], S. K. Li[31], T. Li[9], N. Massari[32], A. Melo[33,34,35], M. Meneghetti[11,12], M. Millon[36], L. Moustakas[37], C. Olave[38], H. Qu[22], K. Rojas[39], C. Saulder[4,3], D. Sluse[6], G. Smadja[40], H. Srivastava[41], A. Sonnenfeld[42,43], C. J. Storfer[44], T. T. Thai[45], C. Tortora[46], N. Wielders[1], Y. Xie[47], B. Altieri[48], A. Amara[49], S. Andreon[50], N. Auricchio[11], C. Baccigalupi[51,52,53,54], M. Baldi[38,11,12], S. Bardelli[11], P. Battaglia[11], R. Bender[4,3], A. Biviano[52,51], M. Bolzonella[11], E. Branchini[55,56,50], M. Brescia[57,46], S. Camera[58,59,60], V. Capobianco[60], C. Carbone[15], V. F. Cardone[61,62], J. Carretero[63,64], M. Castellano[61], G. Castignani[11], S. Cavuoti[46,65], K. C. Chambers[44], A. Cimatti[66], C. Colodro-Conde[67], G. Congedo[68], C. J. Conselice[69], L. Conversi[70,48], Y. Copin[71], A. Costille[26], H. M. Courtois[72], M. Cropper[73], H. Degaudenzi[25], G. De Lucia[52], C. Dolding[73], H. Dole[74], F. Dubath[25], X. Dupac[48], S. Escoffier[75], M. Farina[76], R. Farinelli[11], F. Faustini[61], S. Ferriol[71], M. Frailis[52], E. Franceschi[11], M. Fumana[15], L. Gabarra[8], S. Galeotta[52], K. George[77], B. Gillis[68], C. Giocoli[11,12], P. Gómez-Alvarez[78,48], J. Gracia-Carpio[4], A. Grazian[79], F. Grupp[4,3], L. Guzzo[80,50,81], W. G. Hartley[25], S. V. H. Haugan[82], S. Hemmati[22], H. Hoekstra[83], M. S. Holliman[68], W. Holmes[84], I. M. Hook[85], F. Hormuth[86], A. Hornstrup[87,88], M. Huertas-Company[67,89,90], K. Jahnke[91], M. Jhabvala[92], S. Kermiche[75], A. Kiessling[84], B. Kubik[71], M. Kümmel[3], M. Kunz[36], H. Kurki-Suonio[14,93], A. M. C. Le Brun[94], D. Le Mignant[26], S. Ligori[60], P. B. Lilje[82], V. Lindholm[14,93], I. Lloro[95], M. Magliocchetti[76], G. Mainetti[96], D. Maino[80,15,81], O. Mansutti[52], S. Marcin[39], O. Marggraf[97], M. Martinelli[61,62], N. Martinet[26], F. Marulli[10,11,12], R. J. Massey[98], N. Mauri[66,12], E. Medinaceli[11], S. Mei[99,100], M. Melchior[2], E. Merlin[79], G. Meylan[101], P. Monaco[102,52,53,51], A. Mora[103], M. Moresco[10,11], C. Moretti[52,51,53], L. Moscardini[10,11,12], R. Nakajima[97], C. Neissner[104,64], R. C. Nichol[49], S.-M. Niemi[105], C. Padilla[104], S. Paltani[25], F. Pasian[52], W. J. Percival[106,107,108], V. Pettorino[105], A. Pezzotta[50], G. Polenta[109], L. A. Popa[110], L. Pozzetti[11], F. Raison[4], A. Renzi[111,112,11], J. Rhodes[84], G. Riccio[46], I. Risso[55,56,50], E. Romelli[52], M. Roncarelli[11], B. Rusholme[22], R. Saglia[3,4], Z. Sakr[113,114,115], D. Sapone[116], B. Sartoris[4,52], M. Schirmer[91], P. Schneider[97], T. Schrabback[117], A. Secroun[75], E. Sihvola[118], C. Sirignano[111,112], G. Sirri[12], J. Skottfelt[119], L. Stanco[112], P. Tallada-Crespí[63,64], A. N. Taylor[68], I. Tereno[120,121], N. Tessore[73], S. Toft[122,123], R. Toledo-Moreo[124,125], F. Torradeflot[64,63], A. Tsyganov[126], I. Tutusaus[127,128,114], J. Valiviita[14,93], T. Vassallo[52,77], A. Veropalumbo[50,56,55], Y. Wang[22], J. Weller[3,4], A. Zacchei[52,51], G. Zamorani[11], E. Zucca[11], M. Ballardini[24,129,11], P. Bergamini[11], S. Borgani[102,51,52,53,130], E. Bozzo[25], C. Burigana[21,131], R. Cabanac[114], M. Calabrese[132,15], A. Cappi[133,11], F. Caro[61], T. Castro[134,52,51], D. Di Ferdinando[12], J. A. Escartin Vigo[4], J. García-Bellido[113], T. Gasparetto[61], C. M. Gutierrez[67,135], A. Loureiro[136,137], J. Macias-Perez[138], R. Maoli[139,61], A. A. Nucita[140,141,142], M. Pöntinen[14], E. Sarpa[52], V. Scottez[143,144], M. Sereno[11,12], M. Tenti[12], M. Tucci[25], M. Wiesmann[82], J. A. Acevedo Barroso[84], Y. Akrami[113,145], I. T. Andika[3], G. Angora[46,24], S. Anselmi[112,111,146], M. Archidiacono[80,81], G. Aricò[12], F. Atrio-Barandela[147], M. Baes[7], L. Bazzanini[24,11], D. Bertacca[111,79,112], M. Bethermin[148], F. Beutler[68], L. Blot[149,94], M. L. Brown[69], S. Bruton[150], A. Calabro[61], B. Camacho Quevedo[51,54,52], C. S. Carvalho[121], F. Cogato[10,11], A. R. Cooray[151], P. Corcho-Caballero[28], B. Csizi[117], O. Cucciati[11], T. de Boer[44], G. Desprez[28], A. Díaz-Sánchez[152], S. Di Domizio[55,56], J. M. Diego[31], P.-A. Duc[148], V. Duret[75], M. Y. Elkhashab[52,53,102,51], A. Enia[11], Y. Fang[3], A. Farina[50,56], A. Finoguenov[14], A. Fontana[61], A. Franco[140,141,142], Y. Fu[83,28], K. Ganga[99], E. Gaztanaga[127,128,9], Z. Ghaffari[52,51], F. Giacomini[12], F. Gianotti[11], G. Gozaliasl[153,14], A. Gruppuso[11,12], M. Guidi[38,11], A. Hall[68], N. A. Hatch[154], T. Heuberger[39], H. Hildebrandt[155], J. Hjorth[156], M. Jauzac[157,98,158,159,114], J. J. E. Kajava[160,13,161], Y. Kang[117], V. Kansal[162,163], D. Karagiannis[24,164], J. Kim[8], C. C. Kirkpatrick[118], A. Kovács[165,166], I. Kovačić[7], K. Koyama[9], S. Kruk[48], M. C. Lam[68], M. Lattanzi[129], G. Leroy[157,98], G. F. Lesci[10,11], J. Lesgourgues[167], L. Linke[117], S. J. Liu[76], G. Maggio[52], E. A. Magnier[44], F. Mannucci[168], F. R. Marleau[117], C. J. A. P. Martins[169,170], M. Migliaccio[171,172], M. Miluzio[48,173], G. Morgante[11], K. Naidoo[9,91], A. Navarro-Alsina[97], S. Nesseris[113], L. Nicastro[11], M. Oguri[174,175], F. Oppizzi[56,112,111], F. Pace[58,59,60,176], D. Paoletti[11,131], F. Passalacqua[112], K. Paterson[91], L. Patrizii[12], C. Pattison[9], A. Pisani[75], D. Potter[177], G. W. Pratt[178], S. Quai[10,11], M. Radovich[79], G. Rodighiero[111,79], W. Roster[4], M. Sahlén[179], D. B. Sanders[44], A. Schneider[177], D. Sciotti[61,62], E. Sellentin[180,83], S. Serjeant[181], L. C. Smith[29], I. Szapudi[44], M. Talia[10,11], K. Tanidis[182], C. Tao[75], G. Testera[56], R. Teyssier[183], S. Tosi[55,50,56], A. Troja[52], C. Uhlemann[184,1], C. Valieri[12], D. Vergani[11], G. Vernardos[20,185], P. Vielzeuf[75], E. Vilenius[73], S. Vinciguerra[26], M. von Wietersheim-Kramsta[98,157], N. A. Walton[29], L. Wang[186,28], J. Wilde[16], A. H. Wright[155], and D. Scott[41]

[1] School of Mathematics, Statistics and Physics, Newcastle University, Herschel Building, Newcastle-upon-Tyne, NE1 7RU, UK
[2] University of Applied Sciences and Arts of Northwestern Switzerland, School of Engineering, 5210 Windisch, Switzerland
[3] Universitäts-Sternwarte München, Fakultät für Physik, Ludwig-Maximilians-Universität München, Scheinerstr. 1, 81679 München, Germany
[4] Max Planck Institute for Extraterrestrial Physics, Giessenbachstr. 1, 85748 Garching, Germany
[5] Max-Planck-Institut für Astrophysik, Karl-Schwarzschild-Str. 1, 85748 Garching, Germany
[6] STAR Institute, University of Liège, Quartier Agora, Allée du six Août 19c, 4000 Liège, Belgium
[7] Universiteit Gent, Department of Physics and Astronomy, Proeftuinstraat 86 N3, 9000 Ghent, Belgium
[8] Department of Physics, University of Oxford, Keble Road, Oxford OX1 3RH, UK
[9] Institute of Cosmology and Gravitation, University of Portsmouth, Portsmouth PO1 3FX, UK
[10] Dipartimento di Fisica e Astronomia "Augusto Righi" - Alma Mater Studiorum Università di Bologna, via Piero Gobetti 93/2, 40129 Bologna, Italy
[11] INAF-Osservatorio di Astrofisica e Scienza dello Spazio di Bologna, Via Piero Gobetti 93/3, 40129 Bologna, Italy
[12] INFN-Sezione di Bologna, Viale Berti Pichat 6/2, 40127 Bologna, Italy
[13] Finnish Centre for Astronomy with ESO (FINCA), Quantum, Vesilinnantie 5, University of Turku, 20014 Turku, Finland
[14] Department of Physics, P.O. Box 64, University of Helsinki, 00014 Helsinki, Finland
[15] INAF-IASF Milano, Via Alfonso Corti 12, 20133 Milano, Italy
[16] Institut de Ciències del Cosmos (ICCUB), Universitat de Barcelona (IEEC-UB), Martí i Franquès 1, 08028 Barcelona, Spain
[17] Institució Catalana de Recerca i Estudis Avançats (ICREA), Passeig de Lluís Companys 23, 08010 Barcelona, Spain
[18] Institut de Ciencies de l'Espai (IEEC-CSIC), Campus UAB, Carrer de Can Magrans, s/n Cerdanyola del Vallés, 08193 Barcelona, Spain
[19] CUNY Graduate Center, City University of New York, 365 5th Ave., New York, NY 10016, USA
[20] Department of Physics and Astronomy, Lehman College of the CUNY, Bronx, NY 10468, USA
[21] INAF, Istituto di Radioastronomia, Via Piero Gobetti 101, 40129 Bologna, Italy
[22] Caltech/IPAC, 1200 E. California Blvd., Pasadena, CA 91125, USA
[23] Laboratoire univers et particules de Montpellier, Université de Montpellier, CNRS, 34090 Montpellier, France
[24] Dipartimento di Fisica e Scienze della Terra, Università degli Studi di Ferrara, Via Giuseppe Saragat 1, 44122 Ferrara, Italy
[25] Department of Astronomy, University of Geneva, ch. d'Ecogia 16, 1290 Versoix, Switzerland
[26] Aix-Marseille Université, CNRS, CNES, LAM, Marseille, France
[27] Institut d'Astrophysique de Paris, UMR 7095, CNRS, and Sorbonne Université, 98 bis boulevard Arago, 75014 Paris, France
[28] Kapteyn Astronomical Institute, University of Groningen, PO Box 800, 9700 AV Groningen, The Netherlands
[29] Institute of Astronomy, University of Cambridge, Madingley Road, Cambridge CB3 0HA, UK
[30] Kavli Institute for Cosmology Cambridge, Madingley Road, Cambridge, CB3 0HA, UK
[31] Instituto de Física de Cantabria, Edificio Juan Jordá, Avenida de los Castros, 39005 Santander, Spain
[32] Laboratoire d'Astrophysique de Marseille, Pôle de l'Etoile Site de Château-Gombert 38, rue Frédéric Joliot-Curie, 13388 Marseille cédex 13, France
[33] European Southern Observatory, Karl-Schwarzschild-Str. 2, 85748 Garching, Germany
[34] Departamento de Física, Universidad de Santiago de Chile, Av. Victor Jara 3493, Santiago, Chile
[35] Center for Interdisciplinary Research in Astrophysics Space Science (CIRAS), Universidad de Santiago, Chile
[36] Université de Genève, Département de Physique Théorique and Centre for Astroparticle Physics, 24 quai Ernest-Ansermet, CH-1211 Genève 4, Switzerland
[37] NASA Jet Propulsion Laboratory, California Institut of Technology - 4800 Oak Grove Drive - Pasadena, California 91109, USA
[38] Dipartimento di Fisica e Astronomia, Università di Bologna, Via Gobetti 93/2, 40129 Bologna, Italy
[39] University of Applied Sciences and Arts of Northwestern Switzerland, School of Computer Science, 5210 Windisch, Switzerland
[40] Institut de Physique des 2 Infinis de Lyon, Domaine Scientifique de La Doua - 43, bd du 11 Novembre 1918, 69622 Villeurbanne cédex, France
[41] Department of Physics and Astronomy, University of British Columbia, Vancouver, BC V6T 1Z1, Canada
[42] Department of Astronomy, School of Physics and Astronomy, Shanghai Jiao Tong University, Shanghai 200240, China
[43] Shanghai Key Laboratory for Particle Physics and Cosmology, Shanghai 200240, China
[44] Institute for Astronomy, University of Hawaii, 2680 Woodlawn Drive, Honolulu, HI 96822, USA
[45] National Astronomical Observatory of Japan, 2-21-1 Osawa, Mitaka, Tokyo 181-8588, Japan
[46] INAF-Osservatorio Astronomico di Capodimonte, Via Moiariello 16, 80131 Napoli, Italy
[47] Max-Planck-Institut für Astrophysik, Karl-Schwarzschild-Str. 1 - 85741 Garching, Germany
[48] ESAC/ESA, Camino Bajo del Castillo, s/n., Urb. Villafranca del Castillo, 28692 Villanueva de la Cañada, Madrid, Spain
[49] School of Mathematics and Physics, University of Surrey, Guildford, Surrey, GU2 7XH, UK
[50] INAF-Osservatorio Astronomico di Brera, Via Brera 28, 20122 Milano, Italy
[51] IFPU, Institute for Fundamental Physics of the Universe, via Beirut 2, 34151 Trieste, Italy
[52] INAF-Osservatorio Astronomico di Trieste, Via G. B. Tiepolo 11, 34143 Trieste, Italy
[53] INFN, Sezione di Trieste, Via Valerio 2, 34127 Trieste TS, Italy
[54] SISSA, International School for Advanced Studies, Via Bonomea 265, 34136 Trieste TS, Italy
[55] Dipartimento di Fisica, Università di Genova, Via Dodecaneso 33, 16146, Genova, Italy
[56] INFN-Sezione di Genova, Via Dodecaneso 33, 16146, Genova, Italy
[57] Department of Physics "E. Pancini", University Federico II, Via Cinthia 6, 80126, Napoli, Italy
[58] Dipartimento di Fisica, Università degli Studi di Torino, Via P. Giuria 1, 10125 Torino, Italy
[59] INFN-Sezione di Torino, Via P. Giuria 1, 10125 Torino, Italy
[60] INAF-Osservatorio Astrofisico di Torino, Via Osservatorio 20, 10025 Pino Torinese (TO), Italy
[61] INAF-Osservatorio Astronomico di Roma, Via Frascati 33, 00078 Monteporzio Catone, Italy
[62] INFN-Sezione di Roma, Piazzale Aldo Moro, 2 - c/o Dipartimento di Fisica, Edificio G. Marconi, 00185 Roma, Italy
[63] Centro de Investigaciones Energéticas, Medioambientales y Tecnológicas (CIEMAT), Avenida Complutense 40, 28040 Madrid, Spain
[64] Port d'Informació Científica, Campus UAB, C. Albareda s/n, 08193 Bellaterra (Barcelona), Spain
[65] INFN – Sezione di Napoli, Via Cinthia 6, 80126, Napoli, Italy
[66] Dipartimento di Fisica e Astronomia "Augusto Righi" - Alma Mater Studiorum Università di Bologna, Viale Berti Pichat 6/2, 40127 Bologna,

Italy
[67] Instituto de Astrofísica de Canarias, E-38205 La Laguna, Tenerife, Spain
[68] Institute for Astronomy, University of Edinburgh, Royal Observatory, Blackford Hill, Edinburgh EH9 3HJ, UK
[69] Jodrell Bank Centre for Astrophysics, Department of Physics and Astronomy, University of Manchester, Oxford Road, Manchester M13 9PL, UK
[70] European Space Agency/ESRIN, Largo Galileo Galilei 1, 00044 Frascati, Roma, Italy
[71] Université Lyon 1, CNRS/IN2P3, IP2I Lyon, Villeurbanne, France
[72] Université Lyon 1, CNRS/IN2P3, IUF, IP2I Lyon, Villeurbanne, France
[73] Mullard Space Science Laboratory, University College London, Holmbury St Mary, Dorking, Surrey RH5 6NT, UK
[74] Université Paris-Saclay, CNRS, Institut d'astrophysique spatiale, 91405, Orsay, France
[75] Aix-Marseille Université, CNRS/IN2P3, CPPM, Marseille, France
[76] INAF-Istituto di Astrofisica e Planetologia Spaziali, via del Fosso del Cavaliere, 100, 00100 Roma, Italy
[77] University Observatory, LMU Faculty of Physics, Scheinerstr. 1, 81679 Munich, Germany
[78] FRACTAL S.L.N.E., calle Tulipán 2, Portal 13 1A, 28231, Las Rozas de Madrid, Spain
[79] INAF-Osservatorio Astronomico di Padova, Via dell'Osservatorio 5, 35122 Padova, Italy
[80] Dipartimento di Fisica "Aldo Pontremoli", Università degli Studi di Milano, Via Celoria 16, 20133 Milano, Italy
[81] INFN-Sezione di Milano, Via Celoria 16, 20133 Milano, Italy
[82] Institute of Theoretical Astrophysics, University of Oslo, P.O. Box 1029 Blindern, 0315 Oslo, Norway
[83] Leiden Observatory, Leiden University, Einsteinweg 55, 2333 CC Leiden, The Netherlands
[84] Jet Propulsion Laboratory, California Institute of Technology, 4800 Oak Grove Drive, Pasadena, CA, 91109, USA
[85] Department of Physics, Lancaster University, Lancaster, LA1 4YB, UK
[86] Felix Hormuth Engineering, Goethestr. 17, 69181 Leimen, Germany
[87] Technical University of Denmark, Elektrovej 327, 2800 Kgs. Lyngby, Denmark
[88] Cosmic Dawn Center (DAWN), Denmark
[89] Université PSL, Observatoire de Paris, Sorbonne Université, CNRS, LERMA, 75014, Paris, France
[90] Université Paris-Cité, 5 Rue Thomas Mann, 75013, Paris, France
[91] Max-Planck-Institut für Astronomie, Königstuhl 17, 69117 Heidelberg, Germany
[92] NASA Goddard Space Flight Center, Greenbelt, MD 20771, USA
[93] Helsinki Institute of Physics, Gustaf Hällströmin katu 2, University of Helsinki, 00014 Helsinki, Finland
[94] Laboratoire d'etude de l'Univers et des phenomenes eXtremes, Observatoire de Paris, Université PSL, Sorbonne Université, CNRS, 92190 Meudon, France
[95] SKAO, Jodrell Bank, Lower Withington, Macclesfield SK11 9FT, UK
[96] Centre de Calcul de l'IN2P3/CNRS, 21 avenue Pierre de Coubertin 69627 Villeurbanne Cedex, France
[97] Universität Bonn, Argelander-Institut für Astronomie, Auf dem Hügel 71, 53121 Bonn, Germany
[98] Department of Physics, Institute for Computational Cosmology, Durham University, South Road, Durham, DH1 3LE, UK
[99] Université Paris Cité, CNRS, Astroparticule et Cosmologie, 75013 Paris, France
[100] CNRS-UCB International Research Laboratory, Centre Pierre Binétruy, IRL2007, CPB-IN2P3, Berkeley, USA
[101] Institute of Physics, Laboratory of Astrophysics, Ecole Polytechnique Fédérale de Lausanne (EPFL), Observatoire de Sauverny, 1290 Versoix, Switzerland
[102] Dipartimento di Fisica - Sezione di Astronomia, Università di Trieste, Via Tiepolo 11, 34131 Trieste, Italy
[103] Telespazio UK S.L. for European Space Agency (ESA), Camino bajo del Castillo, s/n, Urbanizacion Villafranca del Castillo, Villanueva de la Cañada, 28692 Madrid, Spain
[104] Institut de Física d'Altes Energies (IFAE), The Barcelona Institute of Science and Technology, Campus UAB, 08193 Bellaterra (Barcelona), Spain
[105] European Space Agency/ESTEC, Keplerlaan 1, 2201 AZ Noordwijk, The Netherlands
[106] Waterloo Centre for Astrophysics, University of Waterloo, Waterloo, Ontario N2L 3G1, Canada
[107] Department of Physics and Astronomy, University of Waterloo, Waterloo, Ontario N2L 3G1, Canada
[108] Perimeter Institute for Theoretical Physics, Waterloo, Ontario N2L 2Y5, Canada
[109] Space Science Data Center, Italian Space Agency, via del Politecnico snc, 00133 Roma, Italy
[110] Institute of Space Science, Str. Atomistilor, nr. 409 Măgurele, Ilfov, 077125, Romania
[111] Dipartimento di Fisica e Astronomia "G. Galilei", Università di Padova, Via Marzolo 8, 35131 Padova, Italy
[112] INFN-Padova, Via Marzolo 8, 35131 Padova, Italy
[113] Instituto de Física Teórica UAM-CSIC, Campus de Cantoblanco, 28049 Madrid, Spain
[114] Institut de Recherche en Astrophysique et Planétologie (IRAP), Université de Toulouse, CNRS, UPS, CNES, 14 Av. Edouard Belin, 31400 Toulouse, France
[115] Université St Joseph; Faculty of Sciences, Beirut, Lebanon
[116] Departamento de Física, FCFM, Universidad de Chile, Blanco Encalada 2008, Santiago, Chile
[117] Universität Innsbruck, Institut für Astro- und Teilchenphysik, Technikerstr. 25/8, 6020 Innsbruck, Austria
[118] Department of Physics and Helsinki Institute of Physics, Gustaf Hällströmin katu 2, University of Helsinki, 00014 Helsinki, Finland
[119] Centre for Electronic Imaging, Open University, Walton Hall, Milton Keynes, MK7 6AA, UK
[120] Departamento de Física, Faculdade de Ciências, Universidade de Lisboa, Edifício C8, Campo Grande, PT1749-016 Lisboa, Portugal
[121] Instituto de Astrofísica e Ciências do Espaço, Faculdade de Ciências, Universidade de Lisboa, Tapada da Ajuda, 1349-018 Lisboa, Portugal
[122] Cosmic Dawn Center (DAWN)
[123] Niels Bohr Institute, University of Copenhagen, Jagtvej 128, 2200 Copenhagen, Denmark
[124] Universidad Politécnica de Cartagena, Departamento de Electrónica y Tecnología de Computadoras, Plaza del Hospital 1, 30202 Cartagena, Spain
[125] European University of Technology EUt+, European Union
[126] Centre for Information Technology, University of Groningen, P.O. Box 11044, 9700 CA Groningen, The Netherlands
[127] Institute of Space Sciences (ICE, CSIC), Campus UAB, Carrer de Can Magrans, s/n, 08193 Barcelona, Spain
[128] Institut d'Estudis Espacials de Catalunya (IEEC), Edifici RDIT, Campus UPC, 08860 Castelldefels, Barcelona, Spain

[129] Istituto Nazionale di Fisica Nucleare, Sezione di Ferrara, Via Giuseppe Saragat 1, 44122 Ferrara, Italy
[130] ICSC - Centro Nazionale di Ricerca in High Performance Computing, Big Data e Quantum Computing, Via Magnanelli 2, Bologna, Italy
[131] INFN-Bologna, Via Irnerio 46, 40126 Bologna, Italy
[132] Astronomical Observatory of the Autonomous Region of the Aosta Valley (OAVdA), Loc. Lignan 39, I-11020, Nus (Aosta Valley), Italy
[133] Université Côte d'Azur, Observatoire de la Côte d'Azur, CNRS, Laboratoire Lagrange, Bd de l'Observatoire, CS 34229, 06304 Nice cedex 4, France
[134] Department of Mathematical Physics, Institute of Physics, University of São Paulo, R. do Matão 1371, 05508-090, São Paulo, SP, Brazil
[135] Universidad de La Laguna, Dpto. Astrofísica, E-38206 La Laguna, Tenerife, Spain
[136] Oskar Klein Centre for Cosmoparticle Physics, Department of Physics, Stockholm University, Stockholm, SE-106 91, Sweden
[137] Astrophysics Group, Blackett Laboratory, Imperial College London, London SW7 2AZ, UK
[138] Univ. Grenoble Alpes, CNRS, Grenoble INP, LPSC-IN2P3, 53, Avenue des Martyrs, 38000 Grenoble, France
[139] Dipartimento di Fisica, Sapienza Università di Roma, Piazzale Aldo Moro 2, 00185 Roma, Italy
[140] Department of Mathematics and Physics E. De Giorgi, University of Salento, Via per Arnesano, CP-I93, 73100, Lecce, Italy
[141] INFN, Sezione di Lecce, Via per Arnesano, CP-193, 73100, Lecce, Italy
[142] INAF-Sezione di Lecce, c/o Dipartimento Matematica e Fisica, Via per Arnesano, 73100, Lecce, Italy
[143] Institut d'Astrophysique de Paris, 98bis Boulevard Arago, 75014, Paris, France
[144] ICL, Junia, Université Catholique de Lille, LITL, 59000 Lille, France
[145] CERCA/ISO, Department of Physics, Case Western Reserve University, 10900 Euclid Avenue, Cleveland, OH 44106, USA
[146] Laboratoire Univers et Théorie, Observatoire de Paris, Université PSL, Université Paris Cité, CNRS, 92190 Meudon, France
[147] Departamento de Física Fundamental. Universidad de Salamanca. Plaza de la Merced s/n. 37008 Salamanca, Spain
[148] Université de Strasbourg, CNRS, Observatoire astronomique de Strasbourg, UMR 7550, 67000 Strasbourg, France
[149] Center for Data-Driven Discovery, Kavli IPMU (WPI), UTIAS, The University of Tokyo, Kashiwa, Chiba 277-8583, Japan
[150] California Institute of Technology, 1200 E California Blvd, Pasadena, CA 91125, USA
[151] Department of Physics & Astronomy, University of California Irvine, Irvine CA 92697, USA
[152] Departamento Física Aplicada, Universidad Politécnica de Cartagena, Campus Muralla del Mar, 30202 Cartagena, Murcia, Spain
[153] Department of Computer Science, Aalto University, PO Box 15400, Espoo, FI-00 076, Finland
[154] School of Physics and Astronomy, University of Nottingham, University Park, Nottingham NG7 2RD, UK
[155] Ruhr University Bochum, Faculty of Physics and Astronomy, Astronomical Institute (AIRUB), German Centre for Cosmological Lensing (GCCL), 44780 Bochum, Germany
[156] DARK, Niels Bohr Institute, University of Copenhagen, Jagtvej 155, 2200 Copenhagen, Denmark
[157] Department of Physics, Centre for Extragalactic Astronomy, Durham University, South Road, Durham, DH1 3LE, UK
[158] Astrophysics Research Centre, University of KwaZulu-Natal, Westville Campus, Durban 4041, South Africa
[159] School of Mathematics, Statistics & Computer Science, University of KwaZulu-Natal, Westville Campus, Durban 4041, South Africa
[160] Department of Physics and Astronomy, Vesilinnantie 5, University of Turku, 20014 Turku, Finland
[161] Serco for European Space Agency (ESA), Camino bajo del Castillo, s/n, Urbanizacion Villafranca del Castillo, Villanueva de la Cañada, 28692 Madrid, Spain
[162] ARC Centre of Excellence for Dark Matter Particle Physics, Melbourne, Australia
[163] Centre for Astrophysics & Supercomputing, Swinburne University of Technology, Hawthorn, Victoria 3122, Australia
[164] Department of Physics and Astronomy, University of the Western Cape, Bellville, Cape Town, 7535, South Africa
[165] MTA-CSFK Lendület Large-Scale Structure Research Group, Konkoly-Thege Miklós út 15-17, H-1121 Budapest, Hungary
[166] Konkoly Observatory, HUN-REN CSFK, MTA Centre of Excellence, Budapest, Konkoly Thege Miklós út 15-17. H-1121, Hungary
[167] Institute for Theoretical Particle Physics and Cosmology (TTK), RWTH Aachen University, 52056 Aachen, Germany
[168] INAF-Osservatorio Astrofisico di Arcetri, Largo E. Fermi 5, 50125, Firenze, Italy
[169] Centro de Astrofísica da Universidade do Porto, Rua das Estrelas, 4150-762 Porto, Portugal
[170] Instituto de Astrofísica e Ciências do Espaço, Universidade do Porto, CAUP, Rua das Estrelas, PT4150-762 Porto, Portugal
[171] Dipartimento di Fisica, Università di Roma Tor Vergata, Via della Ricerca Scientifica 1, Roma, Italy
[172] INFN, Sezione di Roma 2, Via della Ricerca Scientifica 1, Roma, Italy
[173] HE Space for European Space Agency (ESA), Camino bajo del Castillo, s/n, Urbanizacion Villafranca del Castillo, Villanueva de la Cañada, 28692 Madrid, Spain
[174] Center for Frontier Science, Chiba University, 1-33 Yayoi-cho, Inage-ku, Chiba 263-8522, Japan
[175] Department of Physics, Graduate School of Science, Chiba University, 1-33 Yayoi-Cho, Inage-Ku, Chiba 263-8522, Japan
[176] Instituto de Astrofísica e Ciências do Espaço, Faculdade de Ciências, Universidade de Lisboa, Campo Grande, 1749-016 Lisboa, Portugal
[177] Department of Astrophysics, University of Zurich, Winterthurerstrasse 190, 8057 Zurich, Switzerland
[178] Université Paris-Saclay, Université Paris Cité, CEA, CNRS, AIM, 91191, Gif-sur-Yvette, France
[179] Theoretical astrophysics, Department of Physics and Astronomy, Uppsala University, Box 524, 751 20 Uppsala, Sweden
[180] Mathematical Institute, University of Leiden, Einsteinweg 55, 2333 CA Leiden, The Netherlands
[181] School of Physical Sciences, The Open University, Milton Keynes, MK7 6AA, UK
[182] Center for Astrophysics and Cosmology, University of Nova Gorica, Nova Gorica, Slovenia
[183] Department of Astrophysical Sciences, Peyton Hall, Princeton University, Princeton, NJ 08544, USA
[184] Fakultät für Physik, Universität Bielefeld, Postfach 100131, 33501 Bielefeld, Germany
[185] American Museum of Natural History, Department of Astrophysics, New York, NY 10024, USA
[186] SRON Netherlands Institute for Space Research, Landleven 12, 9747 AD, Groningen, The Netherlands

⋆ e-mail: James.Nightingale@newcastle.ac.uk

Appendix A: Forward model, linear inversion, and likelihood

This appendix specifies the calculation underlying the three fits in Sect. 4.5. The joint treatment of MGE lens light and source light follows H24, within the semi-linear framework of Warren & Dye (2003) and Suyu et al. (2006). We describe mesh placement, interpolation, and regularisation separately, since these choices differ between implementations. The related COWLS-I analysis (Nightingale et al. 2025) used MGE light models and cross regularisation, but interpolated its pixelised source using Voronoi natural neighbours.

A.1. Image formation and pixel integration

Let d_i and n_i denote the measured intensity and noise standard deviation of image pixel i within the circular analysis mask. We assumed independent Gaussian noise, with covariance $C_{ij} = n_i^2\delta_{ij}$. The data and noise arrays include the contaminant treatment described in Sect. 3; pixels assigned very large noise have negligible weight. For angular image coordinate $\boldsymbol{\theta}$, the lens equation is

$$\boldsymbol{\beta}(\boldsymbol{\theta};\boldsymbol{\eta}) = \boldsymbol{\theta} - \boldsymbol{\alpha}(\boldsymbol{\theta};\boldsymbol{\eta}) \,, \tag{A.1}$$

where $\boldsymbol{\eta}$ contains the non-linear mass and light parameters, and $\boldsymbol{\alpha}$ includes the SIE and external shear. If L and S are the lens and source surface-brightness distributions, the model image is

$$m_i = \{\mathcal{B}\mathcal{P}[L(\boldsymbol{\theta}) + S(\boldsymbol{\beta}(\boldsymbol{\theta}))]\}_i \,. \tag{A.2}$$

Here $\mathcal{P}$ averages the sampled brightness within each image pixel and $\mathcal{B}$ applies the discrete, normalised PSF convolution, including light from outside the mask that is blurred into fitted pixels. Both operators preserve the intensity convention of the input image.

We evaluated a pixel using a uniform $n_{\mathrm{sub},i}\times n_{\mathrm{sub},i}$ subgrid, averaging the $n_{\mathrm{sub},i}^2$ contributions before PSF convolution. Image-plane subgridding also entered the source mapping in Nightingale et al. (2024), who used 4×4 sampling. Here the sampling varied spatially. In the MGE fit, $n_{\mathrm{sub},i} = 4, 4, 2$ at image-plane radii respectively below $0\farcs1$, between $0\farcs1$ and $0\farcs3$, and above $0\farcs3$ from the data set centre. The same light-profile sampling was retained for the lens MGE in the pixelised fit; the source mapping instead used 4×4 sampling where the adaptation map defined below exceeded a signal-to-noise ratio of three, and 2×2 elsewhere.

For the Sérsic fit, the first-fit mass model defined the source-plane coordinates of the image pixels. Using the same two radial boundaries, sampling was $16, 4, 2$ subpixels per dimension around both the inferred source centre and the lens data set centre, and each image pixel adopted the larger of the two values. Thus the source refinement followed the locations of its lensed images, rather than a single image-plane centre. These sampling maps were set before the corresponding fit.

A.2. MGE basis and joint linear solution

Following the notation of H24, the MGE surface brightness is

$$I_{\mathrm{MGE}}(x,y) = \sum_{k=1}^{N_{\mathrm{g}}^{\mathrm{tot}}} G_k(x,y) \,, \qquad G_k(x,y) = I_k \exp\!\left[-\frac{R_k^2(x,y)}{2\sigma_k^2}\right] \,, \tag{A.3}$$

where $I_k \geq 0$ is the central intensity and σ_k is the major-axis Gaussian width. The elliptical radius and rotated coordinates are

$$R_k^2 = x_k'^2 + (y_k'/q_k)^2 \,, \tag{A.4}$$

$$x_k' = (x - x_k^{\mathrm{c}})\cos\phi_k + (y - y_k^{\mathrm{c}})\sin\phi_k \,, \tag{A.5}$$

$$y_k' = -(x - x_k^{\mathrm{c}})\sin\phi_k + (y - y_k^{\mathrm{c}})\cos\phi_k \,. \tag{A.6}$$

Here q_k is the axis ratio and ϕ_k the orientation of the major axis, measured anticlockwise from the $+x$ axis of the modelling grid. Components within one Gaussian set share their centre, axis ratio, and orientation. The software parameterises each width as $q_k\sigma_k$; these prescribed values were logarithmically spaced from $0\farcs0001$ to the mask radius for both galaxies. There were two sets of 20 lens Gaussians and one set of 20 source Gaussians. The lens sets shared a centre but had independent axis ratios and orientations, giving six non-linear parameters.

At fixed $\boldsymbol{\eta}$, let A_{ik} be the pixel-integrated, PSF-convolved unit-intensity lens profile and f_{ij} the corresponding lensed source mapping, following H24. The source basis consists of Gaussians in the first fit and interpolated mesh functions in the second. With lens intensities $\boldsymbol{I}$ and source intensities $\boldsymbol{S}$, the model is

$$\begin{aligned} m_i &= \sum_j f_{ij}S_j + \sum_k A_{ik}I_k \,, \\ X_{ik} &= \frac{A_{ik}}{n_i} \,, \quad Z_{ij} = \frac{f_{ij}}{n_i} \,, \quad Y_i = \frac{d_i}{n_i} \,. \end{aligned} \tag{A.7}$$

Writing the source regularisation matrix as $\mathsf{H} = \Gamma^{\mathrm{T}}\Gamma$ gives the joint quadratic objective in H24's source-first ordering:

$$Q = \frac{1}{2}\left\|\begin{pmatrix}\mathsf{Z} & \mathsf{X}\\ \Gamma & 0\end{pmatrix}\begin{pmatrix}\boldsymbol{S}\\ \boldsymbol{I}\end{pmatrix} - \begin{pmatrix}\boldsymbol{Y}\\ 0\end{pmatrix}\right\|^2 \,, \qquad S_j \geq 0 \,,\; I_k \geq 0 \,. \tag{A.8}$$

Thus $Q = \frac{1}{2}\chi^2 + \frac{1}{2}\boldsymbol{S}^{\mathrm{T}}\mathsf{H}\boldsymbol{S}$, where χ^2 is the full residual sum defined in Eq. (A.17). The constraints require every source and lens intensity to be non-negative. Without these constraints, the solution obeys

$$\begin{pmatrix}\mathsf{Z}^{\mathrm{T}}\mathsf{Z} + \mathsf{H} & \mathsf{Z}^{\mathrm{T}}\mathsf{X}\\ \mathsf{X}^{\mathrm{T}}\mathsf{Z} & \mathsf{X}^{\mathrm{T}}\mathsf{X}\end{pmatrix}\begin{pmatrix}\widehat{\boldsymbol{S}}\\ \widehat{\boldsymbol{I}}\end{pmatrix} = \begin{pmatrix}\mathsf{Z}^{\mathrm{T}}\boldsymbol{Y}\\ \mathsf{X}^{\mathrm{T}}\boldsymbol{Y}\end{pmatrix} \,. \tag{A.9}$$

All three fits used the `JAX` implementation, which enforces non-negativity using the primal–dual interior-point solver adapted from `JaxNNLS` (Krawczyk 2025),[10] which specialises the `qpax` method of Tracy & Manchester (2024) to non-negative least squares. H24 instead used the modified fast non-negative least-squares algorithm of Bro & De Jong (1997). The off-diagonal blocks couple the lens and source intensities. The lens MGE amplitudes carry no regularisation, corresponding to a zero lens-regularisation block in H24's notation, and $\mathsf{H} = 0$ for the MGE source. For numerical stability, a ridge of 10^{-3} was added to the diagonal of the curvature matrix for each such unregularised amplitude; it entered the linear solve but not χ^2. For adaptive source regularisation, H is the spatially weighted matrix defined below. For the Sérsic stage, each galaxy contributes a unit-intensity Sérsic basis, with shape parameters sampled non-linearly and intensity solved linearly.

A.3. Hilbert placement and Delaunay interpolation

The first MGE fit supplied an adaptation map u_i: the data after subtracting the fitted foreground light, divided by the noise

[10] `https://github.com/CKrawczyk/JaxNNLS`.

map, with values floored at one per cent of the map maximum. This map was held fixed during the pixelised fit. Image-plane mesh placement followed a Hilbert space-filling curve, as also used by He et al. (2025); the weight form below is that of the `PyAutoLens` implementation, with the power and floor chosen for this pipeline. The adaptation map was interpolated along the curve, and the relative sampling weights are

$$w_i^{\mathrm{mesh}} = \max\left[\left(\frac{u_i}{\max_{i'} u_{i'}}\right)^{3.5}, 0.01\right] . \tag{A.10}$$

The weights were normalised and accumulated into a one-dimensional cumulative distribution. Interpolating its inverse at uniformly spaced cumulative weights places more mesh points in high-signal regions while retaining coverage of faint regions. The image-plane vertices were fixed for the fit; their source-plane positions were ray-traced for each trial mass model. We placed 500 points using the Hilbert sampling and added 30 points on a circle just outside the image-plane mask, at radius $r_{\mathrm{mask}} + \Delta\theta/2$, where $\Delta\theta$ is the image pixel scale; the designated boundary amplitudes were constrained to zero. Before interpolation, traced sub-pixels and vertices outside an ellipse fitted to the traced mask border were moved radially onto that ellipse, limiting the influence of rays that would otherwise map to remote source-plane positions.

The traced vertices $\boldsymbol{v}_j$ define a Delaunay triangulation. For a ray landing at $\boldsymbol{\beta}$ in a triangle with vertices $\boldsymbol{v}_1, \boldsymbol{v}_2, \boldsymbol{v}_3$, the barycentric weights satisfy

$$\boldsymbol{\beta} = \sum_{j=1}^{3} b_j \boldsymbol{v}_j , \qquad \sum_{j=1}^{3} b_j = 1 , \qquad S(\boldsymbol{\beta}) = \sum_{j=1}^{3} b_j S_j . \tag{A.11}$$

This is the three-vertex linear interpolation of Vegetti & Koopmans (2009), explicitly described as barycentric interpolation by Vernardos & Koopmans (2022). For image pixel i, its unconvolved mapping matrix is

$$M_{ij} = \frac{1}{n_{\mathrm{sub},i}^2} \sum_{s=1}^{n_{\mathrm{sub},i}^2} b_j(\boldsymbol{\beta}_{is}) , \qquad \mathsf{f} = \mathcal{B}\mathsf{M} , \tag{A.12}$$

where $\boldsymbol{\beta}_{is}$ is the traced position of subpixel s, with zero weights for vertices outside the enclosing triangle. Queries outside the triangulation use the nearest vertex. Intensities therefore reside at vertices and the model is continuous and piecewise linear within the mesh. Assigning one colour to each triangle in the source-plane plots is a display convention and does not describe the interpolation used to fit the image. H24 and COWLS-I (Nightingale et al. 2025) instead used Voronoi natural-neighbour interpolation; Hilbert placement does not require either choice of interpolant.

A.4. Adaptive split regularisation

We used an adaptive cross, or split, regularisation following the approach of Nightingale et al. (2024) and H24, also used in COWLS-I (Nightingale et al. 2025), here evaluated with the Delaunay interpolant. Regularising each vertex against its mesh neighbours makes the number of regularisation terms change whenever a small change in the mass model re-wires the traced mesh, producing discontinuities in the likelihood surface; the cross keeps exactly four terms per vertex, a motivation set out in appendix A.2 ('Likelihood surface noise') of H24. The implementation differs from Nightingale et al. (2024) in its cross geometry: they placed cross points on the diagonals at a distance $\sqrt{\mathcal{A}_j}$, whereas we used the Cartesian axes and half that distance. For vertex j, define its associated area $\mathcal{A}_j$ as one-third of the summed areas of triangles sharing that vertex. Four cross points were placed at

$$\boldsymbol{v}_j \pm h_j \hat{\boldsymbol{x}} , \quad \boldsymbol{v}_j \pm h_j \hat{\boldsymbol{y}} , \qquad h_j = \tfrac{1}{2}\sqrt{\mathcal{A}_j} , \tag{A.13}$$

indexed by $a = 1, \ldots, 4$. Let ω_{jal} be the interpolation weight of source vertex l at cross point (j, a), and $D_{(j,a)l} = \delta_{jl} - \omega_{jal}$. Then

$$\boldsymbol{S}^{\mathrm{T}}\mathsf{H}\boldsymbol{S} = \sum_j \sum_{a=1}^{4} \lambda_j \left[S_j - \sum_l \omega_{jal} S_l\right]^2 + \epsilon \sum_j S_j^2 , \qquad \epsilon = 10^{-8} . \tag{A.14}$$

Equivalently, $\mathsf{H} = \mathsf{D}^{\mathrm{T}}\Lambda\mathsf{D} + \epsilon\mathsf{I}$, where $\Lambda_{(j,a),(j,a)} = \lambda_j$. The small diagonal term stabilises the matrix.

The local regularisation strength was determined from the fixed adaptation map projected through the current mapping. Nightingale et al. (2024) instead derived this signal from a previous model of the lensed source. If N_j is the number of subpixel-to-vertex mappings contributing to vertex j, define

$$t_j = \frac{1}{N_j} \sum_{(i,s)\in\mathcal{M}_j} b_j(\boldsymbol{\beta}_{is}) u_i , \qquad \nu_j = \left(\frac{t_j}{\max_l t_l}\right)^p . \tag{A.15}$$

$\mathcal{M}_j$ is the set of subpixel mappings that include vertex j, and $N_j = |\mathcal{M}_j|$. Unmapped vertices have $t_j = 0$. The exponent p controls how rapidly regularisation changes with signal. In the `AdaptSplit` coefficient convention of the `PyAutoLens` implementation,

$$\lambda_j = \left[c_{\mathrm{in}}\nu_j + c_{\mathrm{out}}(1 - \nu_j)\right]^4 . \tag{A.16}$$

The fourth power follows from squaring the interpolated coefficient to form a regularisation weight and squaring that weight when constructing H; in Nightingale et al. (2024) the interpolated weight was linear and entered H squared. The two positive coefficients and p were inferred non-linearly. They allow bright and faint source regions to have different smoothing strengths without changing the linearity of the intensity solution at each evaluation.

A.5. Statistical objective and fit sequence

For the fitted model image, define

$$\chi^2 = \sum_i \frac{(d_i - m_i)^2}{n_i^2} , \qquad \ln\mathcal{L}_{\mathrm{img}} = -\frac{1}{2}\left[\chi^2 + \sum_i \ln(2\pi n_i^2)\right] . \tag{A.17}$$

The MGE and Sérsic stages used this Gaussian image likelihood evaluated at the non-negative linear solution. For the pixelised stage, the statistical objective additionally accounts for regularisation and source complexity (Suyu et al. 2006; Nightingale et al. 2024; He et al. 2024):

$$-2\ln\mathcal{E} = \chi^2 + \widehat{\boldsymbol{S}}^{\mathrm{T}}\mathsf{H}\widehat{\boldsymbol{S}} + \ln\det(\mathsf{Z}^{\mathrm{T}}\mathsf{Z} + \mathsf{H}) - \ln\det\mathsf{H} + \sum_i \ln(2\pi n_i^2) . \tag{A.18}$$

Table A.1. Quantities fitted and fixed in the three VIS modelling stages.

Stage	Non-linear parameters	Fixed quantities	Linear solution
MGE	Lens and source MGE geometry; SIE and shear	Gaussian widths	Lens and source Gaussian intensities; no regularisation
Pixelised	SIE and shear; adaptive regularisation	First-fit lens MGE geometry; adaptation map and image-plane mesh	Lens Gaussian intensities and source vertex intensities; split regularisation on source
Sérsic	Lens and source Sérsic shapes	First-fit SIE and shear	Lens and source intensities; no regularisation

Here the determinant matrices are the source blocks used by the implementation; the unregularised lens-light amplitudes are excluded from these determinants, although they enter the joint solution and χ^2. The reconstruction imposes the designated zero-amplitude boundary constraints; the determinant calculation retains the source block. This specifies the objective evaluated by the code, not an exact marginalisation over all non-negative lens and source intensities: no additional integration over the positivity-truncated domain was performed.

The candidate conjugate points introduced during preprocessing also constrain the fit. If $\Delta_{\rm pos}$ is their maximum pairwise separation after ray tracing to the source plane and $\delta_{\rm pos}$ is the allowed threshold, the positional penalty subtracted from the log objective is

$$P_{\rm pos} = 10^8 \max(0, \Delta_{\rm pos} - \delta_{\rm pos}) \,, \tag{A.19}$$

with separations expressed in arcseconds. For the first fit, a prefit check removed candidate points within $0''.15$ of the lens-light centre and, where needed, a single outlier, then fitted an SIE with external shear (centre fixed at the lens-light centre) to find the smallest achievable maximum source-plane separation s. The threshold was $\min[\max(2s, 0''.3), 0''.5]$; candidates with fewer than two retained points were fitted without the positional constraint. This discourages configurations in which putative multiple images map to unrelated source locations. In the pixelised fit, the conjugate points were updated from the first-fit model, and the threshold was the larger of three times their first-fit source-plane separation and $0''.2$. This is an auxiliary constraint, rather than an additional independent photometric measurement.

The non-linear sampler explored the mass and free light-shape parameters, and the regularisation parameters when present. With their adopted prior density $\pi(\boldsymbol{\eta})$, the sampled density is proportional to $\mathcal{E}(\boldsymbol{\eta}) \exp[-P_{\rm pos}]\pi(\boldsymbol{\eta})$ for the pixelised fit, replacing $\mathcal{E}$ by $\mathcal{L}_{\rm img}$ for the analytic fits and setting $P_{\rm pos} = 0$ where no positional constraint was supplied. The quantity $\mathcal{E}$ is the per-model inversion objective; it is distinct from the evidence obtained by the outer sampler integrating over non-linear parameters. Table A.1 summarises which quantities change between stages. As in the multiband analysis of COWLS-I (Nightingale et al. 2025), subsequent photometric fits can hold the reference-band mass model fixed. Our NISP and EXT fits were performed independently using the fixed VIS mass model, with their photometric results presented in ECLIPSE-D.

A.6. Priors and stopping criteria

Table A.2 lists the priors for the three VIS fits. We denote a uniform distribution by $\mathcal{U}(a, b)$, a distribution uniform in $\ln x$ by $\mathcal{U}_{\ln}(a, b)$, and a Gaussian with mean m and standard deviation s by $\mathcal{N}(m, s^2)$. The notation $\mathcal{N}_{[a,b]}$ denotes that Gaussian truncated to $[a, b]$. Angular coordinates, radii, and their prior widths are in arcseconds. Each coordinate or ellipticity component receives the listed prior. The data set centre $\boldsymbol{c}_0$ anchors the initial lens-centre priors. For the MGE and SIE shapes, the code sampled ellipticity components $e_0 = [(1 - q)/(1 + q)] \sin(2\phi)$ and $e_1 = [(1 - q)/(1 + q)] \cos(2\phi)$, rather than q and ϕ directly. The two lens MGE sets shared a centre and had independent shape priors, with $e_1^{(1)} > e_1^{(2)}$ imposed to select one labelling of the exchangeable sets. The linear light intensities have non-negativity constraints rather than sampled prior distributions; source-pixel smoothing is specified in Appendix A.4.

The second fit fixed the lens MGE geometry but re-solved its intensities. The SIE parameters were assigned fresh priors, and the shear retained its original prior distributions; neither was narrowed using the first-fit posterior. For the Sérsic fit, centre-prior means were taken from the first-fit posterior medians and the configured standard deviation was $0''.05$. The SIE and shear were fixed to the first-fit maximum-likelihood model. NISP and EXT photometry used that same fixed VIS mass model, as described in Sect. 4.5 and ECLIPSE-D.

We used the `nautilus` convergence criteria (Lange 2023), with exploration ending when the estimated fraction of evidence in the live set fell below $f_{\rm live} = 0.01$. Subsequent sampling required an effective sample size $N_{\rm eff} \geq 500$ and at least one sample in each shell. These are convergence targets, rather than a requirement that the maximum likelihood or estimated evidence cease increasing. Table A.3 gives the live-point counts and maximum likelihood-evaluation budgets. A search could also stop on reaching its evaluation budget before satisfying the convergence targets.

Appendix B: Preliminary round of visual inspection

B.1. Description

A preliminary round of visual inspection was undertaken to determine which diagnostic images are most informative for assessing lens modelling results and to refine the criteria used to judge model success. A random sample of 569 of the 3000 highest machine-learning-ranked (grade A) strong lenses was modelled, and 200 lenses were selected for inspection by 12 classifiers, all of whom identify as lens modelling experts. Each expert reviewed 100 common lenses (to enable consistency checks between reviewers) and 100 unique lenses (to maximise diversity in the identification of failure modes).

In the preliminary round, reviewers were given four images: (i) a 2×2 panel showing RGB images of the lens under different scalings; (ii) a 4×3 panel showing the model fit assuming a Delaunay mesh source; (iii) the same 4×3 panel for a fit assuming an MGE source; and (iv) a 2×1 panel showing the segmentation information of the lens. These images are not shown in this paper for brevity. The number of images and panels given to reviewers

Table A.2. Non-linear priors for the VIS modelling stages. Fixed quantities and linear amplitudes are distinguished from sampled parameters.

Stage	Parameter	Prior or fixed value
MGE	Lens MGE centre, c_k	$\mathcal{U}(c_{0,k} - 0.1, c_{0,k} + 0.1)$
	Lens MGE ellipticity, each set	$\mathcal{N}_{[-0.5,0.5]}(0, 0.3^2)$
	Source MGE centre, c_k	$\mathcal{N}(c_{0,k}, 0.3^2)$
	Source MGE ellipticity	$\mathcal{N}_{[-0.7,0.7]}(0, 0.3^2)$
	SIE centre	Fixed to $\boldsymbol{c}_0$
MGE/pixelised	SIE ellipticity	$\mathcal{N}_{[-1,1]}(0, 0.3^2)$
	SIE scale $\theta_{\rm E}^{\rm mass}$	$\mathcal{U}(0, 8)$
	Shear components $\gamma_1^{\rm ext}, \gamma_2^{\rm ext}$	$\mathcal{U}(-0.3, 0.3)$
Pixelised	SIE centre, c_k	$\mathcal{U}(c_{0,k} - 0.1, c_{0,k} + 0.1)$
	Lens MGE geometry	Fixed to first-fit maximum-likelihood values
	$c_{\rm in}, c_{\rm out}$	$\mathcal{U}_{\ln}(10^{-6}, 10^{6})$
	Signal exponent p	$\mathcal{U}(0, 1)$
Sérsic	Lens/source centre, c_k	$\mathcal{N}(\bar{c}_k^{\rm MGE}, 0.05^2)$
	Lens/source ellipticity	$\mathcal{N}_{[-1,1]}(0, 0.3^2)$
	Lens/source effective radius	$\mathcal{U}(0, 30)$
	Lens Sérsic index	$\mathcal{U}(0.5, 10)$
	Source Sérsic index	$\mathcal{U}(0.8, 5)$
	SIE and shear	Fixed to first-fit maximum-likelihood values

Table A.3. `Nautilus` settings for the three VIS searches.

Fit	Live points	Evaluation limit
MGE	750	200 000
Pixelised	300	100 000
Sérsic	100	100 000

was intentionally larger than would be practical for evaluating 15 072 strong lenses. The motivation was to determine what information reviewers needed to judge lenses.

Reviewers first assessed all 200 lenses with three classification options corresponding to SC, FL, and MGL, indicating whether the lens model was considered successful. Reviewers were provided with an evaluation panel, which gave the following criteria for a model to be considered successful:

1. You have high confidence the data set is of a genuine strong lens.
2. The pixelated lens model accurately fits all multiple images of the lensed source, and does not fit light of other nearby galaxies or foreground lens light residuals.
3. The pixelated lens model provides an accurate and publication-worthy estimate of the Einstein radius.
4. There are no issues with the segmentation map.
5. The lens does not have multiple galaxies inside its Einstein radius and thus does not require multiple lens light and mass components.

A failed model was defined as one or more of the above criteria not being met, and the MGL option was used when criterion 5 was not met. After classifying all 200 objects, reviewers were subsequently shown all results again for lenses they classified as failures. Next to each image shown to reviewers were buttons they could click to identify the reason for the failure. For example, next to the segmentation image was a button labelled "Missing Nearby Artefact/Galaxy", meaning the segmentation had not correctly enabled masking of the nearby galaxy. Another button next to the fit panel was labelled "Bad Source Reconstruction".

The third and final round of inspection asked reviewers to click on the image panels that allowed them to determine whether a lens model was SC or FL. This information was analysed to determine the final images (Figs. 1 and 2) that were actually shown to reviewers for inspection of the full sample of 15 072 lenses.

B.2. Discussion and lessons learned

Reviewers agreed that judging whether a lens model is successful is inherently subjective, and that it would be impossible to define assessment criteria interpreted identically by all inspectors. However, it was also agreed that the criteria used during the preliminary visual inspection were unnecessarily complicated, particularly because they mixed assessment of the lens model itself with assessment of the segmentation map, including criteria such as "does not fit light from nearby galaxies" or "there are no issues with the segmentation map". It was therefore decided that segmentation-map validation – specifically checking whether genuine source emission had been removed or nearby contaminating galaxies had not been identified correctly – would be performed separately from the primary visual inspection and not included directly in the model-success criteria.

The inspection criteria were subsequently simplified to those presented in Sect. 5, with the revised structure more directly guiding inspectors towards the appropriate classification, including identifying MGL systems before assessing model quality. Reviewers agreed that the refined criteria still retained some subjectivity, but substantially less than in the preliminary inspection exercise.

During the preliminary inspection, reviewers first classified all 200 lenses and only afterwards returned to failed systems to record the reason for failure. Inspectors noted that this often led to them forgetting why a particular model had been classified as

unsuccessful. The final inspection workflow therefore required reviewers to select the failure category immediately after selecting FL. The available failure categories were also simplified to the set described in Sect. 5.

Finally, the diagnostic images used during inspection were analysed and refined into the layouts shown in Figs. 1 and 2. Discussion amongst reviewers motivated the option to alternate between pixelised and parametric MGE source reconstructions, which provides valuable additional diagnostic information for difficult or ambiguous systems.

Appendix C: Additional SC examples

Figure 3 compares three grade A models with current SC-vote fractions of 100%, 75%, and 50%. Figure C.1 adds 14 grade A systems drawn randomly from the current inspection results. Every selected system has exactly four recorded votes: three have $4/4$ SC votes, four have $3/4$, and seven have $2/4$. The draws excluded the Figure 3 candidate set and contained no repeated objects. They were restricted to locally available completed pixelised fits and RGB images registered to the VIS cut-outs. The four-vote restriction applies to these illustrative examples, not to the entire inspection export.

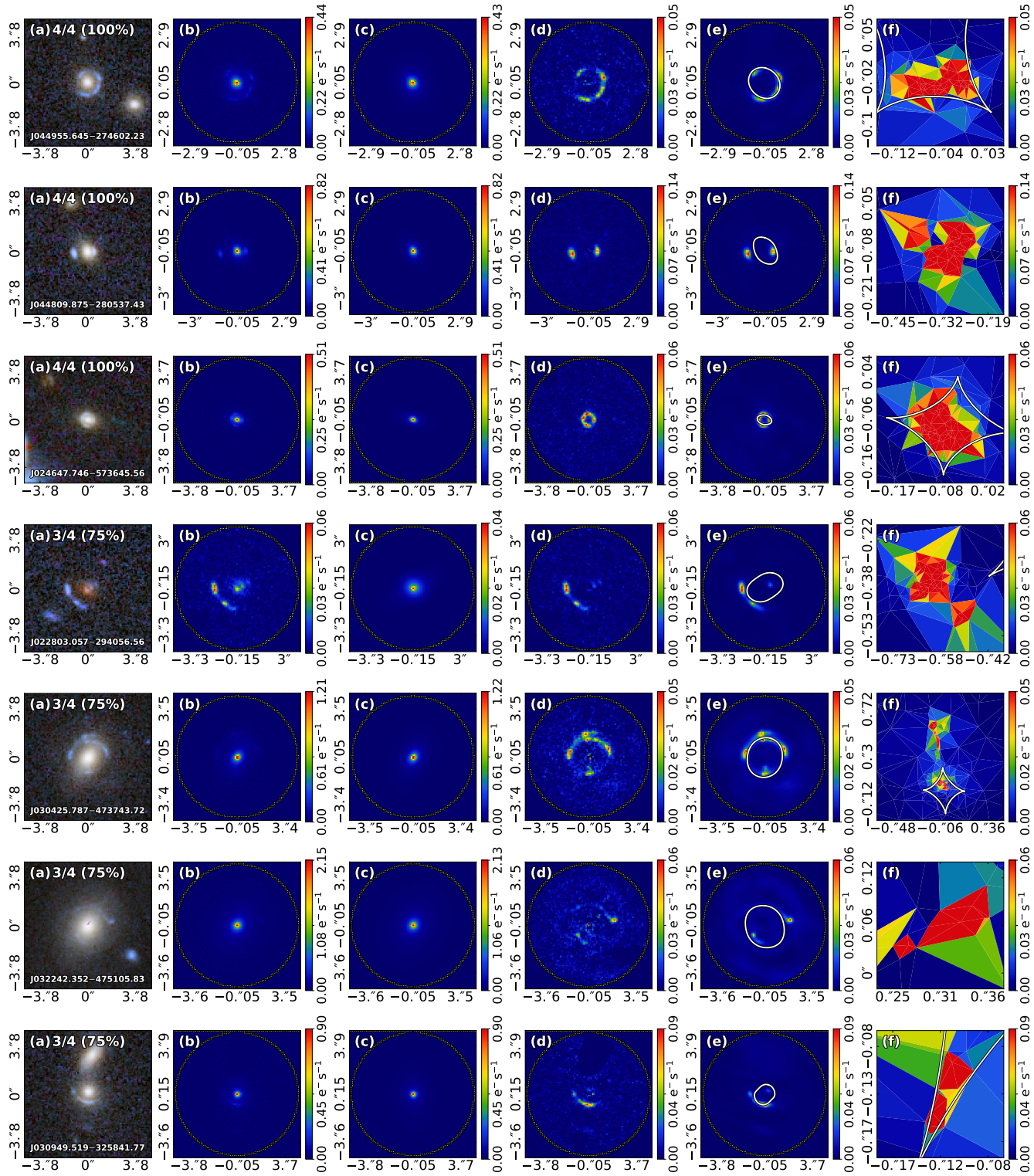


Fig. C.1. Additional randomly selected grade A lens models from the current inspection campaign. The first three rows have 4/4 (100%) SC votes and the remaining four have 3/4 (75%). All seven meet the adopted 75% SC threshold. Each RGB panel gives the SC-vote tally and percentage. All panels are shown north up, east left. From left to right, the panels show the RGB image (a), VIS data (b), foreground lens-light model (c), lens-subtracted image (d), lensed source-model image (e), and source-plane reconstruction (f), following Fig. 3. These examples illustrate model appearance and are not a statistical calibration of model reliability.

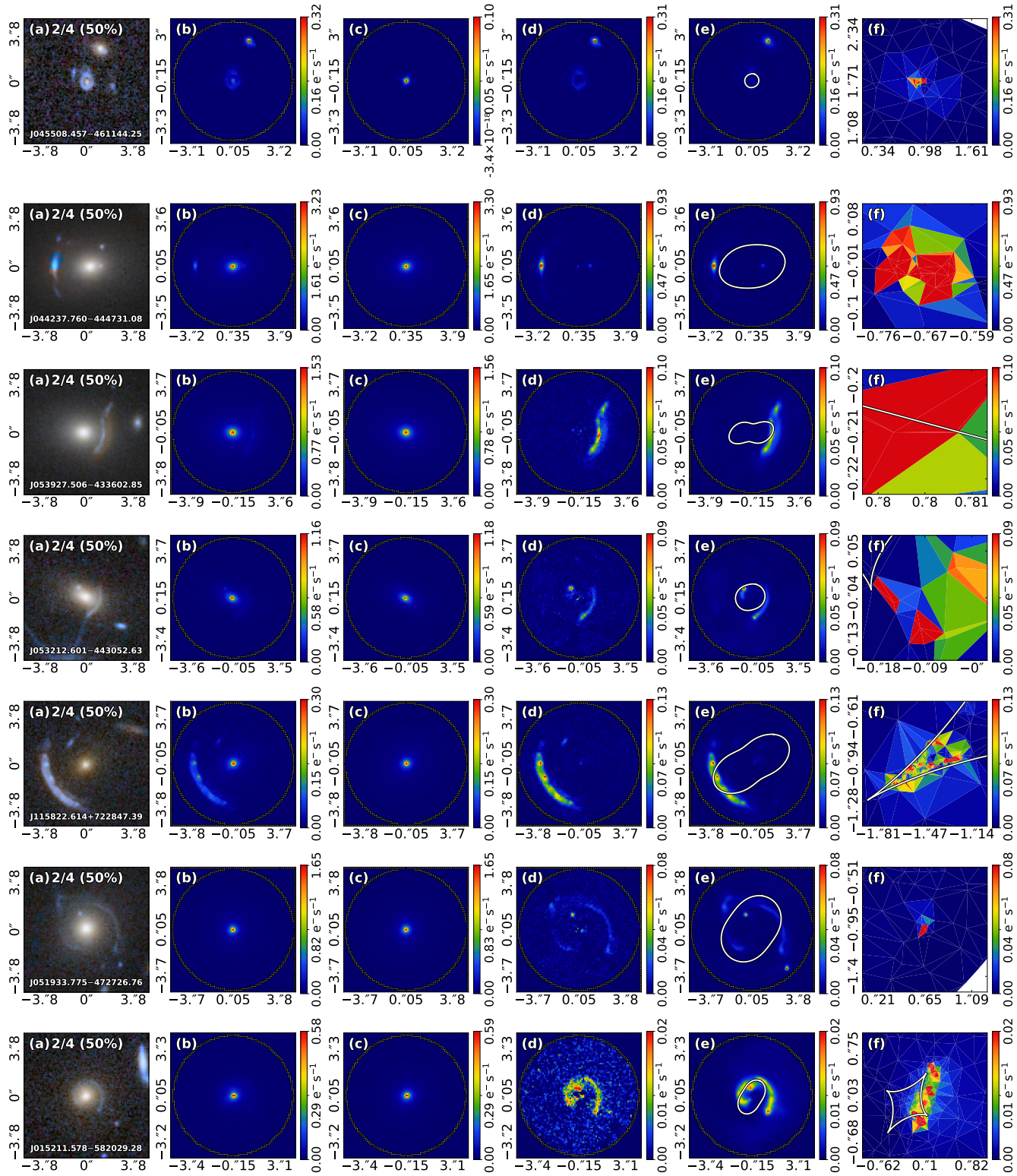


Fig. C.1 (continued). Additional randomly selected grade A lens models from the current inspection campaign, each with exactly 2/4 (50%) SC votes. All seven are NC at the adopted 75% threshold. Each RGB panel gives the observed SC-vote tally and percentage. All panels are shown north up, east left. Panels follow the layout of Fig. 3. These lower-agreement examples provide a qualitative comparison with the 100% and 75% examples, rather than a calibration of classification reliability.